



**HAL**  
open science

# Assessment of discrete wind gust parameters: Towards the worst-case scenario of a FSI application in form of an inflated hemisphere

Guillaume de Nayer, Michael Breuer

► **To cite this version:**

Guillaume de Nayer, Michael Breuer. Assessment of discrete wind gust parameters: Towards the worst-case scenario of a FSI application in form of an inflated hemisphere. *Journal of Wind Engineering and Industrial Aerodynamics*, 2022, 231, pp.105207. 10.1016/j.jweia.2022.105207 . hal-03836356

**HAL Id: hal-03836356**

**<https://hal.science/hal-03836356>**

Submitted on 2 Nov 2022

**HAL** is a multi-disciplinary open access archive for the deposit and dissemination of scientific research documents, whether they are published or not. The documents may come from teaching and research institutions in France or abroad, or from public or private research centers.

L'archive ouverte pluridisciplinaire **HAL**, est destinée au dépôt et à la diffusion de documents scientifiques de niveau recherche, publiés ou non, émanant des établissements d'enseignement et de recherche français ou étrangers, des laboratoires publics ou privés.



Distributed under a Creative Commons Attribution 4.0 International License



# Assessment of discrete wind gust parameters: Towards the worst-case scenario of a FSI application in form of an inflated hemisphere

G. De Nayer, M. Breuer\*

Professur für Strömungsmechanik, Helmut-Schmidt-Universität Hamburg, D-22043 Hamburg, Germany

## ARTICLE INFO

### Keywords:

Wind gust  
Fluid–structure interaction (FSI)  
Worst-case scenario  
Turbulent flow  
Large-eddy simulation (LES)  
Meta-model

## ABSTRACT

The paper is a step towards the evaluation of the worst-case scenario caused by strong wind gusts impacting civil engineering air-inflated lightweight structures. These extreme events with short durations but high strengths are responsible for short-term highly instantaneous loads endangering the structural integrity of the design. For this purpose, a generic test case is defined which includes a discrete wind gust model, the approaching turbulent boundary layer and a flexible structure exposed to the resulting fluid flow. The simulation framework relies on a partitioned coupled solver for fluid–structure interaction extended by two source-term formulations which allow to inject the wind gusts as well as the background turbulence. To save CPU time, a part of the investigations is conducted for the rigid case as a physical meta-model. The particularly critical cases found in this way were examined for the case of the flexible structure. Under varying system parameters such as the strength, length and position of the gust the following objective functions are evaluated: Force coefficients, maximal deflections and local inner stresses. The worst case occurs for maximal gust strength and length, when the gust hits the membrane at half height. Furthermore, the effect of the superposition of the discrete gust with background turbulence is analyzed for two scenarios. The gust is first superimposed to different inflow turbulences of the same intensity leading to non-negligible deviations of force coefficients and deflections. Second, the level of the turbulence intensity is successively increased up to a factor of five showing only a minor effect on the flexible structure not generating a new worst case.

## 1. Introduction

In civil engineering wall-mounted hemispherical structures are numerous (silos, tents, stadium, ...). Their design requires attention to prevent failures occurring in the material. Despite their simple geometry, the flow around these structures is complex and the occurring fluid–structure interaction (FSI) leads to two types of failures: The first is fatigue appearing as the initiation and propagation of cracks in the material due to cyclic loading (Kemper, 2022). The second failure occurs when a critical load is reached, the so-called *worst-case scenario*. Material fatigue is a research topic on its own. The dedicated literature is vast (see, e.g., Schijve, 2003) and this topic will not be tackled here. Contrary to fatigue the determination of the worst case is less documented, at least for numerical predictions.

The complexity of the flow around hemispherical structures is demonstrated in Wood et al. (2016), where a rigid wall-mounted hemisphere plunged into a turbulent boundary layer is experimentally and numerically investigated. Subsequently, the noteworthy FSI phenomena occurring at a flexible membranous structure inflated in form of a hemisphere are presented based on a measurement campaign (Wood

et al., 2018) and coupled FSI simulations (De Nayer et al., 2018a; Apostolatos et al., 2019). In these studies the approaching flows are boundary layers with different turbulence intensities in the order of 10%. These turbulent fluctuations lead to oscillations of the fluid forces acting on the membrane. Limited in terms of amplitude, these turbulent fluctuations of low strength are important for the investigation of material fatigue, but not for the *worst-case scenario*.

Since in civil engineering the *worst case* is often triggered by wind gusts impacting the structure, the consideration of a realistic representation of the atmospheric boundary layer including extreme events typically with short durations but high strengths is required. In order to realize that, precursor CFD simulations as carried out e.g. by Porté-Agel et al. (2011) are not feasible in the context of determining the worst-case scenario for expensive fully-coupled applications. Another appropriate description of the atmospheric boundary layer relies on synthetic data generated based on a mean velocity profile, turbulence intensities, spectra, length scales and coherence functions (Burton et al., 2001). Often, a power-law approximation is applied for the mean profile. For the generation of turbulent fluctuations the design standards in

\* Corresponding author.

E-mail address: [breuer@hsu-hh.de](mailto:breuer@hsu-hh.de) (M. Breuer).

civil engineering (IEC-Standard, 2002) and in aeronautics (EASA, 2020; FAA, 2014) impose the use of *continuous/stochastic/probabilistic* models. In order to generate time histories of the velocity components at given points, one-dimensional fast Fourier transforms (FFT) are applied on spectra such as von Kármán or Kaimal. These spectra statistically describe the wind for all frequencies and are parametrized by turbulence length scales and intensities. To take the spatial variation of turbulence into account, the spectral description of the wind has to be extended by coherence functions. An advanced method proposed by Mann (1998, 2012) is widely used and part of the IEC-Standards. This model combines the rapid distortion theory and a three-dimensional spectral tensor to represent the turbulent wind flow as homogeneous, stationary, Gaussian and anisotropic. The velocity components are derived simultaneously by applying one three-dimensional FFT, so that the correlations among these components directly satisfy reference data. These well-established continuous models offer a realistic three-dimensional representation of the wind which inherently includes gusts. Therefore, they are commonly used in civil and wind engineering (Sørensen et al., 2002; Andersen and Sørensen, 2018; Doubrawa et al., 2019; Kelly et al., 2021) and aeronautics (Patil, 2007; Fonte et al., 2015). Furthermore, since the statistical description of severe wind events changes over the duration of a storm, the consideration of non-stationary, non-homogeneous and non-Gaussian processes is of a great significance for the stochastic modeling of wind load (Kareem, 2008; Kareem and Wu, 2013).

*Continuous gust* models are applied in the context of fatigue evaluation (De Jonge and Vink, 1997; Reytier et al., 2012), but more rarely for the determination of extreme loads. For example, Michalski et al. (2015) studied the fluid–structure interaction of a large umbrella structure in an atmospheric boundary layer. To describe the natural wind conditions upstream of the structure in form of multi-correlated wind velocity time series, the inflow conditions are synthetically generated based on the method developed by Mann (1998) and refined by Michalski et al. (2011). A clear drawback of this methodology is that due to the fact that the (coupled) simulations are extremely CPU-time consuming, typically only simulations lasting over a period of 10 min could be carried out. This limited duration of the dynamic simulation leads to a high uncertainty for the determination of the extreme response under wind load. A repetition of the simulations with three different sets of transient inflow boundary conditions can reduce the risk of missing the worst-case scenario, but also increases the CPU-time requirements significantly.

Another probabilistic methodology to forecast wind gusts is based on in-situ wind-speed measurements. For example, Wang et al. (2020, 2022) applied several probabilistic approaches based on machine learning models and sparse Gaussian regression using wind-speed measurements to predict wind fields. Although these models are intended to forecast short-term (0–6 h ahead) and long-term (7–24 h ahead) time series, the predictions are solely for time histories at singular locations and are not sufficient to describe the local structure of a wind gust required for CFD predictions. Therefore, they will not be considered further.

Another category of wind gust models, which are also part of the design standards, are the *discrete* gust models (Hoblitt, 1988; Wu et al., 2019). They are less realistic but deterministic and offer a good alternative for the worst-case determination in the context of a computational framework in the time domain like in the present study. In *discrete* models the gust is directly described by a mathematical function representing its velocity over time (e.g., 1-cosine shape, also known as Extreme Coherent Gust (ECG), IEC-Standard, 2002). This description of a gust is simplistic and does not integrate any turbulence information. To overcome this issue, a common manner is to superimpose *discrete* gusts on a realistic turbulent background flow generated with prescribed turbulence length scales and intensities (Storey et al., 2014). In aeronautics the *discrete* model is one of the standard methods to study the aeroelastic response of a wing (Sitaraman and Baeder,

2006; Wales et al., 2014; Zholtoviski et al., 2020) or a complete airplane (Raveh, 2011; Huntley et al., 2017; Heinrich and Reimer, 2017). However, it is also applied in civil engineering. For example, Norris et al. (2010) and Storey et al. (2013) studied the effects of wind gusts on wind turbines and their wake based on an actuator-disk and LES. Furthermore, Santo et al. (2020) and Piquee et al. (2022) investigate the deformations of rigid or elasto-flexible membrane blades of a wind turbine exposed to a discrete gust based on a coupled URANS-FEM approach. Similar to the present study, a deterministic ECG-type of gust is applied.

To include the determination of the *worst-case scenario* for a deformable structure exposed to wind is not trivial, since the considered system often has multiple input parameters and output goals. The input parameters can strongly vary generating millions of possibilities. For example, the number of load cases for the airplane model Digital-X evaluated by Knobloch (2015) was about 8 millions for six input parameters. Reviewing the worst-case methods found for discrete gusts and for continuous turbulent gusts, different methodologies are followed in the literature.

In the early 80s the original *statistical discrete gust (SDG)* method appears (Jones, 1973) followed later by simplified versions (Jones, 2004). The SDG combines the continuous turbulence approach with discrete gusts to evaluate the *worst-case scenario* especially for the certification of aircrafts by the Federal Aviation Administration. The SDG can be applied to nonlinear aircraft systems in combination with a systematic search among different but equiprobable gust patterns to track the *worst-case response*. This search is described by Jones (2009) as a three-steps process composed of a random Monte-Carlo search, followed by a genetic optimization algorithm and terminated by a Nelder–Mead simplex search procedure.

The *Matched Filter Theory (MFT)* is a method taken from signal processing and often applied in aeronautics (Zeiler, 1997). The theory works well for linear systems by taking advantage of the principle of superposition and is valid for a single input/single output system. It is based on convolution integrals and also includes Fourier transformations. The MFT consists of three steps (Scott et al., 1993): First, an impulse function of unit strength is applied to the linear system delivering the impulse response of the considered output goal, i.e., the gust load. Second, this impulse response is normalized by its own energy and reversed in time delivering a matched excitation waveform of unit energy. Third, this waveform is sent to the linear system and its resulting response produces time series and a maximal value. The MFT guarantees that there is no other unit-energy input waveform producing a response value larger than this maximum. In that way the *worst-case scenario* is found. An application of the MFT to determine the worst-case scenario due to a gust is presented in Fidkowski et al. (2008). The extension of the MFT technique to nonlinear systems is possible, but a search procedure is required to determine the excitation waveform that maximizes the response (Scott et al., 1993). For high-fidelity predictions often carried out in the time domain, the MFT possesses the further disadvantage that Fourier transforms are required to switch from the time to the frequency domain.

Another possibility to figure out the worst-case scenario relies on *surrogate or meta-modeling approaches*. Based on a restricted number of simulations for the considered linear or non-linear problem, mathematical relations between input design parameters and output goals are generated in a best possible way. They are denoted *meta-models*. The extrema of these mathematical functions can be derived and thus the worst case can be approximated. An important factor for the meta-model performance is the proper selection of the sampling points. The so-called design of experiments techniques determine this set to get the maximum information with a minimum effort. For example, in order to investigate the response of an aircraft model to the classical 1-cosine gust, Khodaparast et al. (2012) constructed meta-models using different approaches such as the radial basis functions or the Kriging predictor. The number of simulations to build a meta-model is still

high, but negligible compared to the case without such a method. Other applications of meta-models are found in [Fournier et al. \(2019\)](#) applying a second-order polynomial expansion or in [Nazzari et al. \(2015\)](#) using a meta-model relying on artificial neural networks.

As another direction of methodologies *pure optimization techniques without meta-model* can be used to find the worst-case scenario of linear or non-linear systems. Relying on a starting set of samples, new samples are deduced using deterministic or stochastic optimization methods such as hill-climbing, evolutionary or genetic algorithms. The optimization process is continued until the extremum is found, i.e., the worst-case scenario is determined. For example, in [Khodaparast et al. \(2012\)](#) different optimization approaches were applied to search for the critical load response of an aircraft.

Finally, a combination of *meta-models with optimization approaches*, also called Surrogate Based Optimization, seems to be an efficient alternative to evaluate the worst-case scenario. For example, the design explorer algorithm used in [Khodaparast et al. \(2012\)](#) delivers faster results than the pure optimization techniques. The German Aerospace Center used a surrogate model fed by their CFD solver TAU and applied a gradient-based optimization technique for accurately identifying critical load cases ([Ripepi et al., 2018](#); [Goertz et al., 2020](#)). [Guzman Nieto et al. \(2019\)](#) propose a framework based on the efficient global optimization algorithm ([Jones et al., 1998](#)) and the Kriging meta-model to estimate critical dynamic aeroelastic loads. Applying one of these techniques allows to find the worst-case scenario triggered by gusts.

Summarizing the literature review with regard to the intended usage of high-fidelity coupled simulations to find the worst-case scenario of civil engineering FSI applications, meta-models with or without optimization algorithms combined with *discrete gusts* seem to be a highly attractive alternative to continuous gust models more often applied in civil engineering. The former are more common in aeronautic applications but are advantageous especially for investigating short-term events in an efficient manner since solely the time interval of the gust impact has to be taken into account and not long-lasting time series awaiting the appearance of strong gusts. Thus, the study has two main objectives:

1. Transfer and extension of a methodology for investigating the effect of wind gusts on structures from aeronautics to civil engineering
2. Better understanding of the input parameters and output goals of a well-established test case in order to later determine the worst-case scenario with meta-models and optimization

According to the second issue, the following open questions are tackled in this investigation: How many input parameters are relevant in case of discrete wind gusts hitting a flexible membrane? Are some of these parameters linked to each others, so that the list of input parameters can be reduced? Is it possible to use much cheaper CFD simulations of the rigid case as a physical meta-model of the FSI case? Which role does the incoming turbulence play? Furthermore, a deeper insight into the complex behavior should be achieved.

To tackle these issues, Section 2 presents the generic test case including the discrete wind gust model, the approaching stochastic flow and the considered structures. Furthermore, a list of input/output parameters for the worst-case scenario search is defined. The simulation framework is introduced in Section 3 including the fluid and structure solvers, the fluid-structure coupling and the computational setup. Based on the rigid and the flexible cases the influence of different parameters is investigated in Section 4.

## 2. Generic lightweight civil engineering FSI case and reduction of parameters

The present investigation is directed towards the worst-case scenario of civil engineering applications subjected to strong wind gusts. As a major goal the material has to be able to withstand the loads.

Therefore, local stresses and particularly the maximal local stresses are objective functions of the problem. The global force coefficients (force divided by stagnation pressure and reference area) on the structure are also of relevance as well as the maximal deformations. Thus, the typical scenario is as follows. The designed structure, which is a lightweight structure since it is especially prone to dynamic loads, is located in an atmospheric boundary layer. The flow can be characterized by certain boundary layer parameters such as the boundary layer thickness and the turbulence intensity as well as the temporal and spatial length scales of the approaching flow. However, the most critical loads are encountered by short-term, highly dynamic events such as strong wind gusts. In the present case the investigations are restricted to discrete gusts. Nevertheless, that already brings a lot of free parameters into play such as the gust strength, the temporal and spatial length scales of the gust as well as their location. Furthermore, the interaction between the background turbulence and the sporadically occurring wind gust has to be investigated. For this purpose, the following assumptions and simplifications concerning the wind gusts (Section 2.1), the approaching boundary layer (Section 2.2) and the structures (Section 2.3) are taken into account. A sketch of the generic test case is depicted in [Fig. 1](#). The discussion will use dimensionless variables denoted by \*, applying the width of the structure as the reference length (here  $D$ ) and the free-stream velocity  $u_\infty$  as the reference velocity. As an example,  $t^*$  is the dimensionless time such as  $t^* = t u_\infty / D$ .

### 2.1. Discrete wind gusts

The gust shape is deterministically defined in the local basis  $B_1 = (O, \mathbf{g}_1, \mathbf{g}_2, \mathbf{g}_3)$  (see [De Nayer et al., 2022](#), for details about the theory and the basis). Its definition is based on a user-defined strength of the gust  $A_g$  and user-defined analytic functions representing the shape of the gust in time and space. The direction of the gust is the first vector of the local basis  $\mathbf{g}_1$ . Thus, the velocity of the gust in the local basis reads:

$$\mathbf{u}_g|_{B_1}(t, \xi, \eta, \zeta) = A_g f_t(t) f_1(\xi) f_2(\eta) f_3(\zeta) \mathbf{g}_1. \quad (1)$$

The spatial functions ( $f_1, f_2$  and  $f_3$ ) as well as the temporal function  $f_t$  are characterizing the deterministic gust imposed. In the present study solely the Extreme Coherent Gust (ECG) defined in the [IEC-Standard \(2002\)](#) is used. However, instead of applying the original *1-cosine shape* an adapted version ([De Nayer et al., 2019](#)) is considered:

$$f_i(\phi) = \begin{cases} \frac{1}{2} \left( 1 + \cos \left( \frac{2\pi(\phi - \phi_g)}{L_g^\phi} \right) \right) & \text{for } (\phi - \phi_g) \in \left[ -\frac{L_g^\phi}{2}, \frac{L_g^\phi}{2} \right] \\ 0 & \text{else.} \end{cases} \quad (2)$$

which introduces the central value  $\phi_g$  of the gust distribution. This measure allows to achieve more control than for the original ECG shape. Here the variable  $\phi$  is equal to the coordinate  $\phi = \{x, y, z\}$  or the time  $t$  and the subscript  $i$  is equal to 1, 2, 3 or  $t$ , respectively. The length and time scales are denoted  $L_g^\phi$ . In the present case the temporal shape function  $f_t(t)$  follows the same analytical function as the spatial shape  $f_1(\xi)$  oriented in gust direction.

The parameters to be defined are the temporal and spatial scales in each direction. Since the temporal scale is deduced from the spatial length scale in the gust direction with  $L_g^t = L_g^\xi / u_g^{\text{conv}}$ , only three spatial scales are required (i.e.,  $L_g^\xi, L_g^\eta$  and  $L_g^\zeta$ ). To reduce the number of free parameters, the length scales of the gust in wall-normal and spanwise direction are fixed to  $L_g^\eta = L_g^\zeta = 1 D$  ( $D$  = diameter of hemisphere), while that of the gust direction is varied in the range  $0.5 \leq L_g^\xi / D \leq 1.5$  as well as the strength of the gust in the range  $0.5 \leq A_g / u_\infty \leq 1.5$ . The upper strength value of  $A_g / u_\infty = 1.5$  is chosen, because the generated gust for the considered case has a maximal total velocity of  $u_\infty + A_g \approx$

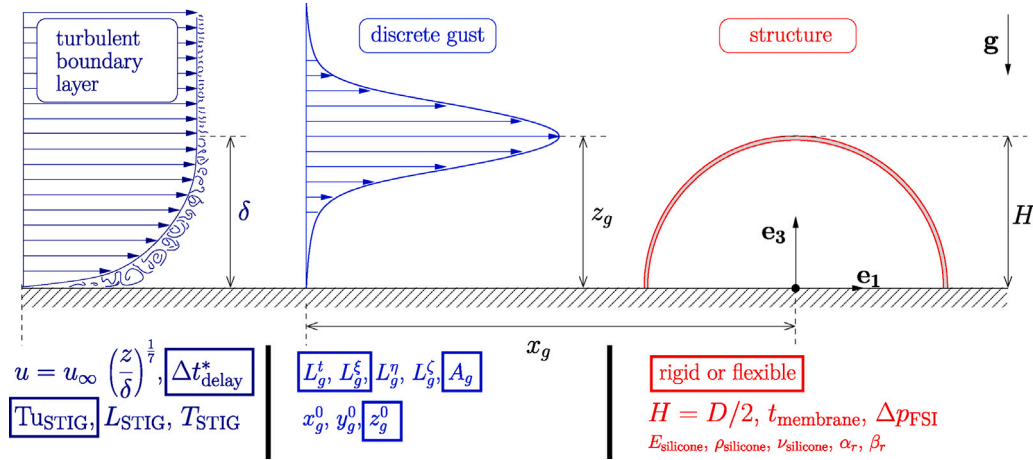


Fig. 1. Generic lightweight civil engineering case with all parameters. The parameters varied within this study are marked by a box. The others are considered to be fixed.

25 m/s (90 km/h). This corresponds to *storm* level as presented in Table A.2. The lower bound  $A_g/u_\infty = 0.5$  leads to a maximal total gust velocity of  $u_\infty + A_g \approx 15$  m/s (54 km/h), which is the first category of wind gust called *near gale*.

The position vector  $(x_g^0, y_g^0, z_g^0)$ , where the gust is initially injected, is also a parameter of the problem.  $y_g^0$  is set to 0, which describes the geometric symmetry plane, so that the gust fully hits the structure of interest in the middle. The position  $x_g^0$  is taken constant near the structure and is determined to  $x_g^0/D = -1.5$  so that the longest gust (largest  $L_g^\xi$ ) can be injected before reaching the bluff body. Contrary to  $x_g^0$  and  $y_g^0$ , the position  $z_g^0$  varies in a limited range between  $2/8D$  and  $5/8D$  to investigate, how the location of the gust center in vertical direction influences the local and global fluid loads on the structure.

The wind gust is injected horizontally and with no angle to the vertical plane  $\mathbf{e}_1 - \mathbf{e}_3$ , i.e., the direction of the gust coincides with the direction of the base flow  $\mathbf{g}_1 = \mathbf{e}_1$ . No angle with the vertical plane  $\mathbf{e}_1 - \mathbf{e}_3$  is assumed due to the symmetric shape of the structure. Furthermore, a zero angle with respect to the horizontal plane  $\mathbf{e}_1 - \mathbf{e}_2$  is set based on the fact that the gust is convected along the ground in the direction of the main flow as in the case of a gust front.

## 2.2. Turbulent boundary layer

The structure of interest is located in a thick turbulent boundary layer. Its characteristics (thickness, turbulence intensities) have a direct influence on the flow around the bluff body (e.g., horseshoe vortices, recirculation area, ...). Since the present study concentrates on the highly transient events and the associated worst-case scenario, except the turbulence intensity these characteristics are not considered as parameters of the problem. Consequently, the distribution of the time-averaged velocity in main flow direction closely follows the 1/7 power law. At a distance of 1.5 diameters upstream of the bluff body the thickness of the boundary layer  $\delta$  corresponds to the height of the hemisphere ( $\delta = D/2$ ) (see Wood et al., 2016). To prescribe a realistic turbulent inflow, synthetic perturbations are injected into the computational domain upstream of the body. These synthetic data are generated using the so-called Synthetic Turbulent Inflow Generator (STIG) relying on the digital filter concept of Klein et al. (2003). For this purpose, the time-averaged velocities and Reynolds stresses measured in the experiment (Wood et al., 2016, 2018) and complemented by DNS data of Schlatter et al. (2009) are taken into account leading to a peak turbulence level of  $Tu_{STIG}^0 = \sqrt{\frac{1}{3}(\overline{u'u'} + \overline{v'v'} + \overline{w'w'})}/u_\infty = 8\%$  close to the bottom wall. Note that this is the standard setup used for most of the cases considered in Section 4, except in Section 4.2.3 where the effect of the turbulence intensity is studied. The other important parameters to be defined are the integral time and length scales, where the digital

filter concept solely allows to set a constant value within the entire boundary layer. As motivated in detail in De Nayer et al. (2022) the integral length scales are assumed to be equal in all directions and set to the following values:  $L_z^{STIG}/D = L_y^{STIG}/D = L^{STIG}/D = 2.04 \times 10^{-2}$ . The dimensionless integral time scale is deduced with the help of the Taylor hypothesis and set to  $T^{STIG} u_\infty/D = 2.85 \times 10^{-2}$ .

## 2.3. Wall-mounted rigid or flexible structure

The investigated structure has a hemispherical shape of diameter  $D$  and is mounted on an uniform smooth wall generating the boundary layer specified above. Based on the free-stream mean velocity  $u_\infty$  in  $x$ -direction at standard atmospheric conditions ( $\rho_{\text{air}} = 1.225 \text{ kg/m}^3$ ,  $\mu_{\text{air}} = 18.27 \times 10^{-6} \text{ kg/(m s)}$ ) the Reynolds number is set to 100,000. For preliminary investigations the structure is assumed to be rigid denoted *rigid case*, whereas the ultimate goal is to study the fluid-structure interaction in case of a membranous flexible structure denoted *flexible case*. With the focus of finding the worst-case scenario, the same membranous material is used in all investigations, and therefore, the material properties are held constant. The thin-walled flexible membrane is made of silicone (Wacker Elastosil 625) according to the experimental setup of Wood et al. (2018). Relying on a St. Venant-Kirchhoff material the density, Young's modulus and Poisson's ratio were determined to  $\rho_{\text{silicone}} = 1050 \text{ kg/m}^3$ ,  $E_{\text{silicone}} = 7 \times 10^5 \text{ Pa}$  and  $\nu_{\text{silicone}} \approx 0.45$ , respectively. For the rubber-type material a certain degree of internal structural damping has to be taken into account to model the energy dissipation in the silicone material. For the purpose that the flexible hemisphere case could be easily reproduced by the FSI community, a convenient and well-established internal structural damping model was employed in De Nayer et al. (2018a). That is taken over here and is given by a Rayleigh damping with the constant mass- and stiffness-proportional parameters set to  $\alpha_r = 17.47$  and  $\beta_r = 1.89 \times 10^{-4}$ . These damping parameters are determined using the Rayleigh method (see Appendix A.2 in De Nayer et al., 2018a) based on additional structural test cases described in Wood et al. (2018). An average thickness of  $t_{\text{membrane}} = 1.65 \times 10^{-4}$  is assumed. The thin-walled membranous structure is pressurized on the inside by air in a form of a hemisphere. The pressure difference  $\Delta p_{\text{FSI}} = p - p_\infty = 43 \text{ Pa}$  between the inner gauge pressure of the structure and the pressure outside is a compromise between stabilization and contour accuracy (Wood et al., 2018). Additionally, the setup is exposed to the gravitational acceleration  $\mathbf{g} = -9.81 \text{ m/s}^2 \mathbf{e}_3$ .

## 2.4. Summary

To tackle the worst-case scenario of a generic lightweight civil engineering case, the global force coefficients, the local stresses in the

**Table 1**  
Varied input parameters of the generic test case.

|                          | Gust strength    | $A_g/u_\infty$              | 0.5, 0.75, 1.0, 1.25, 1.5  |
|--------------------------|------------------|-----------------------------|--|
| Discrete gust            | Gust length      | $L_g^\xi/D$                 | 0.5, 0.75, 1.0, 1.25, 1.5  |
|                          | Gust position    | $z_g^0/D$                   | 2/8, 3/8, 4/8, 5/8   |
| Turbulent boundary layer | Time delay       | $\Delta t_{\text{delay}}^*$ | 0–24   |
|                          | Turbulence level | $Tu_{\text{STIG}}^0$        | $\alpha Tu_{\text{STIG}}^0$ with $\alpha \in \{1, 1.5, 2, 2.5, 3, 5\}$ |
| Structure                | Type             | –                           | Rigid/flexible   |

structure and its maximal deformations are considered as objective functions. According to the detailed explanations above, the following about the system parameters listed in Table 1 can be concluded:

- *Discrete wind gusts:*

Solely the gust strength, the extension of the gust in streamwise direction and the vertical position of the injected gust are chosen as free parameters in this study. The two other characteristic length scales are fixed. Note that different gust strengths are taken into account instead of solely considering the most intense gust to set-up the physical meta-model explained below.

- *Superposition of discrete gusts with inflow turbulence:*

While the properties of the approaching boundary layer are fixed, one important issue remains. When a discrete gust is released at a certain time and superimposed with the background turbulence of the boundary layer, the instant in time at which the superposition takes place is still a free parameter and may influence the resulting loads on the structure. In Table 1 this parameter is denoted time delay  $\Delta t_{\text{delay}}^*$ . Additionally, the effect of a rising turbulence intensity  $Tu_{\text{STIG}}$  is investigated in the current work.

- *Model for the structure:*

Since the effect of strong wind gusts on flexible structures is the final objective, this case is in the focus. However, in order to reduce the high computational effort for fully coupled FSI simulations, the question arises whether a physical meta-model can be set-up based on the less time-consuming case of a rigid structure. That would allow to carry out at least parts of the investigations based on more stable and less CPU-time intensive simulations.

Simulations with  $A_g/u_\infty = 0.5$  or  $L_g^\xi/D = 0.5$  were also carried out. However, the generated gusts are partially too weak and their effects on the force coefficients (min/max) are difficult to track. Therefore, some of the results obtained with  $A_g/u_\infty = 0.5$  or with  $L_g^\xi/D = 0.5$  are skipped in Section 4.

### 3. Simulation framework

#### 3.1. Numerical methods

The finite-volume solver FASTEST-3D is applied (Durst and Schäfer, 1996) for simulating the turbulent fluid flow based on the large-eddy simulation technique. The filtered Navier–Stokes equations are discretized on a curvilinear, block-structured body-fitted grid with a collocated variable arrangement. Standard methods such as a second-order low-storage three substeps Runge–Kutta scheme for the temporal discretization and the midpoint rule with a blended central scheme (5% upwind) for the spatial discretization are applied as in Wood et al. (2016). A semi-implicit predictor–corrector scheme (projection method) of second-order accuracy in space and time is preferred over the standard implicit SIMPLE scheme for the solution of the pressure–velocity coupling problem (Breuer et al., 2012). The large scale are resolved directly, whereas the non-resolvable small scales of the turbulent flow have to be taken into account by a subgrid-scale (SGS) model. The classical (Smagorinsky, 1963) SGS model applying the standard

parameter  $C_s = 0.1$  combined with the Van-Driest damping function is used, since a preliminary study (De Nayer et al., 2018b) has proven that the model delivers reasonable results for this test case.

As described above synthetic turbulent perturbations are injected into the computational domain upstream of the zone of interest based on the source-term method by Schmidt and Breuer (2017), Breuer (2018) and De Nayer et al. (2018b). These synthetic data are generated using the digital filter concept of Klein et al. (2003) and the corresponding input parameters detailed in Section 2.2. In a similar manner as the turbulent fluctuations, the injection of the discrete gusts relies on a recently developed source-term formulation by De Nayer and Breuer (2020) which allows to inject horizontal or head-on wind gusts of different strengths just in front of the flexible structure as shown in De Nayer et al. (2022). That possesses several advantages compared to the far-field boundary condition (Norris et al., 2010; De Nayer et al., 2019), where the gust is introduced as a velocity variation at the inlet of the computational domain. The latter often goes along with numerical dissipation which occurs during the traveling of the gust from the inlet to the zone of interest. Second, this traveling time has to be simulated, which is costly. The first issue can be avoided by the *resolved gust approach* of Heinrich (2014), but the second issue remains. This disadvantage can only be cured by injecting the wind gust close to the zone of interest. Prescribed velocity methods such as the field velocity method (Singh and Baeder, 1997) and the split velocity method (Wales et al., 2014) allow to superimpose strong velocity variations to the base flow anywhere in the computational domain. These methodologies work well for vertical gusts often encountered in aerodynamics. However, as demonstrated in Boulbrachene et al. (2021) they are not an appropriate choice for horizontally/head-on oriented gusts which are of high relevance in civil engineering. Thus, the source-term formulation (De Nayer and Breuer, 2020) is applied here and the gusts are introduced in the vicinity of the rigid or membranous structure.

The simulation framework for the coupled FSI problem is based on a partitioned procedure (Breuer et al., 2012). For this purpose, the fluid solver is coupled with the computational structure dynamics (CSD) solver Carat++ (Bletzinger et al., 2006). The coupling and the mapping between the two diverse surface discretizations at the FSI interface are carried out by the open-source software EMPIRE (Sicklinger et al., 2014). All the data exchange relies on message passing interface (MPI) communications.

Since the FSI simulation framework relies on body-fitted grids, FASTEST-3D is written in the ALE formulation. To describe the fluid motion in temporally varying domains, the fluid grid has to be adapted at each time step. Different techniques are available: In case of small deformations a very fast algebraic procedure is performed based on a combination of linear and transfinite interpolations (TFI) (Thompson et al., 1985). If the deformations become significant, a hybrid adaption method especially developed for FSI problems within LES (Sen et al., 2017) is applied. It relies on a combination of an inverse distance weighting interpolation for the block boundaries of the block-structured grid and a three-dimensional TFI for the inner mesh.

The deformation of the structure due to the fluid loads at the FSI interface is predicted by Carat++. It is a finite-element and an isogeometric solver for the structure developed with emphasis on the prediction of the mechanical behavior of thin-walled structures such as shells and membranes (Breitenberger et al., 2015; Philipp et al., 2016). The momentum equation written in a Lagrangian frame of reference is applied to describe the dynamic equilibrium of the structure. A St. Venant–Kirchhoff material law is assumed and links the Piola–Kirchhoff stress tensor with the Green–Lagrange strain tensor (Basar and Weichert, 2013). The time is discretized relying on the standard second-order non-linear Newmark scheme.

EMPIRE (*Enhanced Multi Physics Interface Research Engine*) is an open-source coupling tool dedicated to co-simulations. It allows to generate own coupling algorithms by writing a user-defined xml input

file. Standard coupling algorithms such as loose or strong staggered schemes or more complex approaches such as Jacobian-based schemes can be easily defined. EMPIRE does the mapping between the non-matching CFD and CSD grids and the exchange of data with its clients. Details about the presently applied mortar mapping in case of FEM discretizations can be found in Wang et al. (2016) and Apostolatos et al. (2019).

### 3.2. Computational setup

The *rigid* case composed of the non-deformable hemisphere is a pure CFD problem. Thus, only the fluid solver is required. The computational domain is a perfect hemispherical expansion in radial direction (radius  $10D$ ) starting from the center of the body. Inside, a block-structured grid is generated containing  $4.3 \times 10^6$  control volumes (CV). Most of the grid points are concentrated near the walls to fully resolve the viscous sublayer (first cell center located at a distance of  $\Delta z/D \approx 5 \times 10^{-5}$  from the wall) and near the structure to resolve the relevant flow phenomena of the considered problem (horseshoe vortices, transition, detachment, vortex shedding, ...). The aspect ratio of the CVs on the body are between 1 and 10 and the geometric stretching ratios in radial direction are kept below 1.1. This *medium* mesh fulfills the recommendations by Piomelli and Chasnov (1996) for wall-resolved LES about the cell sizes in the wall-normal and tangential directions and is chosen to keep the computational effort in case of the *flexible* structure reasonable. Nevertheless, a detailed comparison of the flow obtained on this *medium* grid with the flow predicted on a *fine* mesh can be found in De Nayer et al. (2018b).

No-slip walls are considered at the bottom of the domain and on the surface of the hemispherical structure. The outer hemispherical surface of the computational domain is divided into inlet and outlet patches. For the part of the outlet, where vortical structures are leaving the domain, a convective boundary condition is applied. The convective velocity follows the 1/7 power law according to the inlet. At the other part of the outlet a standard zero velocity-gradient boundary is set.

A total of 960,000 time steps of synthetic turbulent inflow data corresponding to about 30 dimensionless time units are generated in order to provide continuous time histories of the fluctuating incoming flow especially for the investigation presented in Section 4.2.3.

The setup of the fluid part for the *flexible* case is identical to the *rigid* case introduced above. Additionally, the fluid grid is adapted using the fast TFI method to take the deformation of the body into account. The structure part relies on the FEM solver Carat++. The thin-walled structure is modeled by membrane FE elements. Based on the grid independence study carried out in De Nayer et al. (2018a), a grid composed of 1926 *Constant Strain Triangle* (CST) elements and 999 nodes is sufficient. All nodes have three degrees of freedom except the ones connected to the smooth plate at  $z/D = 0$ . These nodes cannot move in any translational direction. Concerning the other CSD boundary conditions, the fluid loads predicted by the fluid solver are solely available for the outer FSI interface of the flexible body. The air flow inside the hemisphere is not taken into account by the fluid solver and the static pressure difference  $\Delta p_{\text{FSI}}$  required for the pressurization of the thin-walled membrane is modeled directly in the CSD solver by a follower pressure load acting on each surface element. The gravitational acceleration is taken into account in Carat++ as a dead load acting on the volume of each element. In order to define the initial state of the membranous structure, a homogeneous and isotropic pre-stress tensor field is prescribed with the value of  $n_{\text{membrane}} = 7794.5$  Pa (see De Nayer et al., 2018a, for the determination of this value).

To predict the *flexible* case correctly, the FSI problem has to converge at each time step. The present computational framework allows a strong coupling by applying FSI sub-iterations. However, since the ratio of the structural density to the fluid density is large ( $\rho_{\text{silicone}}/\rho_{\text{air}} \approx 857$ ), the added-mass effect is very limited for the present configuration. That is the reason why a loose coupling scheme (i.e., the fluid problem and

the structure problem are solved only once per time step) is selected to minimize the data exchange and the grid adaption.

Regarding the temporal discretization, both solvers apply the same time step  $\Delta t^* = \Delta t u_{\infty} / D = 3.317 \times 10^{-5}$ . This value is dictated by the fluid solver leading to a mean value of the CFL number of about  $3 \times 10^{-2}$  (computed with the local velocity and the length of the cell).

## 4. Results

Before discussing the influence of the different input parameters on the objective functions of the test case presented in Section 2, the understanding of the flow physics and the associated FSI phenomena are of high interest. The presentation of the results begins with the flow around the rigid structure under gust load, which is a good foundation for the description of the results for the flexible structure. Note that a more detailed description of the flow including time histories of the velocity and the pressure at fixed monitoring points upstream of the structure can be found in De Nayer et al. (2022).

### 4.1. Rigid structure

#### 4.1.1. Flow physics of the wall-mounted rigid structure

In Section 4.1.2 the streamwise and vertical force coefficients predicted for the rigid case and the constant gust height of  $z_g^0/D = 4/8$  but with different gust strengths  $A_g$  and gust lengths  $L_g^{\xi}$  will be compared. As shown below despite their differences, all curves have two local peaks in  $c_x$  and one local peak in  $c_z$  in common due to the passage of the gust over the hemisphere. In order to explain the governing flow physics relevant for all cases, it is sufficient to describe a single case. For this purpose, the sample encompassing the gust with the parameters  $z_g^0/D = 4/8$ ,  $A_g/u_{\infty} = 1.0$  and  $L_g^{\xi}/D = 1.0$  is selected and depicted in Fig. 2. Please note that this case does not coincide with the *medium gust* simulation presented in De Nayer et al. (2022) which was carried out including turbulent fluctuations at the inflow. This inflow turbulence is omitted here to limit the effects observed in the objective functions to the variation of the input parameters.

In Fig. 2 the time histories of the force coefficients for this specific configuration are compared with a reference simulation without any gust. It is worth mentioning that for the case without gust the force coefficients are still varying in time. The reason for these fluctuations are the complex flow phenomena (horseshoe vortex, separation, shear layer, reattachment, ...) observed at the obstacle and in its wake as described in Wood et al. (2016). For the gust case the dimensionless time  $t^* = 0$  corresponds to the beginning of the gust injection, whereas  $t^* = 1$  defines the end of the injection in the present case of  $L_g^{\xi}/D = 1.0$ .

It is important to mention that both simulations (with and without gust) are initiated by the same restart file, i.e., exactly the same initial conditions. Nevertheless, small deviations in the time histories can already be observed before the gust hits the structure in one of the simulations. The cause for this observation is the fact that the gust is injected close to the structure to limit its traveling time and possible numerical damping effects. Therefore, the front of the gust is not so far from the front of the structure during the injection into the computational domain ( $t^* < 1$ ) and thus already influences the flow upstream of the body, especially the region of the horseshoe vortex. The increase in pressure in this area leads to variations of the force coefficients already before the gust reaches the structure ( $t^* < 1$ ) as visible in Fig. 2.

Shortly after the end of the injection at  $t^* = 1.16$  (point a in Fig. 2(a)), the front of the gust impacts the hemisphere and leads to a local increase of the streamwise force coefficient denoted  $c_x^{\text{max}, 1}$ . The flow corresponding to this time instant is highlighted in Fig. 3(c) depicting the streamwise velocity and in Fig. 3(d) depicting the pressure in the symmetry plane  $y/D = 0$ . In the figure of the streamwise velocity the position of the gust is tracked by the iso-surface  $u_1/u_{\infty} = 1.4$ , whereas this iso-surface is replaced by a black iso-line in the

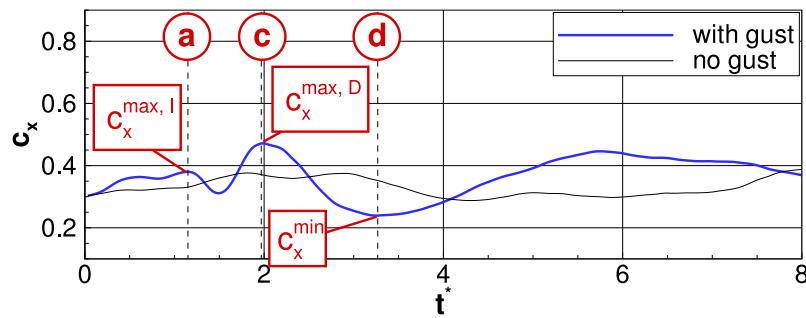
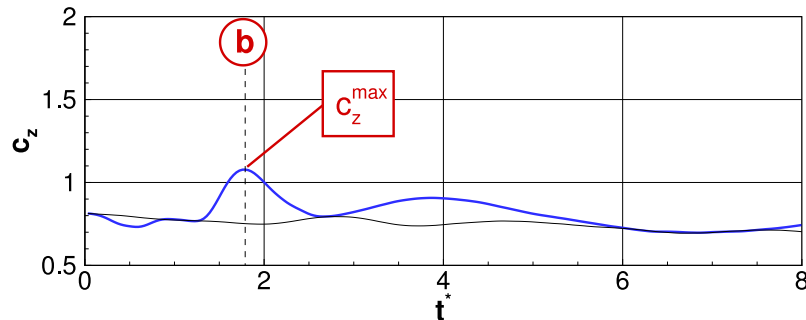
(a) Streamwise force coefficient  $c_x$ .(b) Vertical force coefficient  $c_z$ .

Fig. 2. Rigid case ( $z_g^0/D = 4/8$ ,  $A_g/u_\infty = 1.0$ ,  $L_g^\xi/D = 1.0$ ): Streamwise and vertical force coefficients as a function of the dimensionless time  $t^*$ .

pressure distribution to see the pressure changes hidden behind the gust structure. As expected, the increase of the velocity due to the presence of the gust leads to a local decrease of the pressure at the position of the gust (visible by comparing Fig. 3(d) with Fig. 3(b), which depicts a typical pressure distribution before the gust injection). When the gust hits the hemispherical obstacle, a local zone of high pressure forms at the front of the hemisphere. Since the rest of the flow field (sides and recirculation area behind the bluff body) is not affected at this time instant, it leads to the first local (impact) peak  $c_x^{\max, I}$  in the streamwise force coefficient.

Afterwards, the gust continues to travel downstream. At about  $t^* = 1.79$  (point b in Fig. 2(b)), the gust is located above the hemisphere as depicted in Figs. 3(e) and 3(f). Due to the strong acceleration of the flow close to the tip of the hemisphere, a zone of low pressure forms at the location of the gust. That leads to strong suction pulling the body up and thus the peak of the maximum vertical force coefficient denoted  $c_z^{\max}$ .

Shortly thereafter at  $t^* = 2.0$  (point c in Fig. 2(a)), the gust detaches from the bluff body. This departure has as a consequence an increase of the low pressure region in the recirculation area behind the hemisphere visible in Fig. 3(h). This low pressure area in the back originating from the tip region leads to the second peak in  $c_x$  marked by  $c_x^{\max, D}$ . The second (departure) peak  $c_x^{\max, D}$  is higher than the first (impact) peak  $c_x^{\max, I}$ . Consequently, the departure of the gust from the body has a stronger effect on the objective function  $c_x$  than the gust impact.

Afterwards, the gust continues to travel downstream in the wake with a shape modified by the impact on the hemisphere. Although the gust moves away from the body, its passing continues to be visible in the temporal evolution of the forces. This issue can be observed in Figs. 2(a) and 2(b). Obviously, the streamwise force coefficient  $c_x$  drops to a level, which is below the value of the case without the gust ( $2.5 < t^* < 4$ ), whereas  $c_z$  is still slightly higher than in the case without the gust ( $2.5 < t^* < 6$ ).

At  $t^* \approx 3.28$  (point d in Fig. 2(a)) a minimum  $c_x^{\min}$  is reached. This minimum can be explained by visualizing the flow in Figs. 3(i) and 3(j). The area of low pressure located behind the hemisphere in Figs. 3(d),

3(f) and 3(h) has vanished due to the gust passing. Thereafter, the gust leaves the region of interest. For  $t^* > 8$  the temporal evolutions of the force coefficients predicted for the gust case tend towards those obtained without any gust comparable to the situation before the gust injection ( $t^* < 0$ ) depicted in Figs. 3(a) and 3(b).

#### 4.1.2. Influence of the gust strength $A_g$ , length $L_g^\xi$ and height $z_g^0$ on the resulting fluid forces

For the investigations on the effect of the different gust parameters the simulations are still carried out applying a turbulent boundary layer without turbulent fluctuations, i.e., a constant 1/7 power law. The motivation for this choice is to concentrate on the influence of the gust parameters without any disturbances from the incoming turbulent flow.

In general, the idea is to study the influence of three main gust parameters, i.e., the gust strength  $A_g$ , the gust length  $L_g^\xi$  and the gust height  $z_g^0$ . Thus, the challenging task is to present the output of the simulations depending on these three parameters in a clear way. For this purpose, Figs. 4 and 5 depict the force coefficients for a constant gust height of  $z_g^0/D = 4/8$  in two different manners. Either the gust strength or the gust length is fixed, whereas the other variable varies. Different line patterns denote different gust strengths  $A_g$  and different line colors denote different gust lengths  $L_g^\xi$ . The rise of the two peaks in the streamwise force coefficient  $c_x$  with both the gust strength as well as the gust length can be clearly seen. Obviously, the same is true for the vertical force coefficient  $c_z$ . Similar observations can be made for the cases not shown here, i.e., for gust heights  $z_g^0/D$  lower or higher than 4/8. The increase of the force coefficients with  $A_g$  is easy to understand, while the influence of the gust length  $L_g^\xi$  requires further explanations given below.

To see the trends more clearly, Figs. 6 to 8 depict the maximal force coefficients  $c_x^{\max, I}$ ,  $c_x^{\max, D}$  and  $c_z^{\max}$  in three different representations. First of all, in Fig. 6 the gust strength  $A_g$  is the abscissa, whereas the gust length is taken into account by different lines. The results for different gust heights are shown in separate sub-figures. Obviously, the peak values of  $c_x^{\max, I}$  and  $c_z^{\max}$  increase quadratically with  $A_g$ . Since the kinetic energy of the gust rises according to  $A_g^2$ , this effect on the

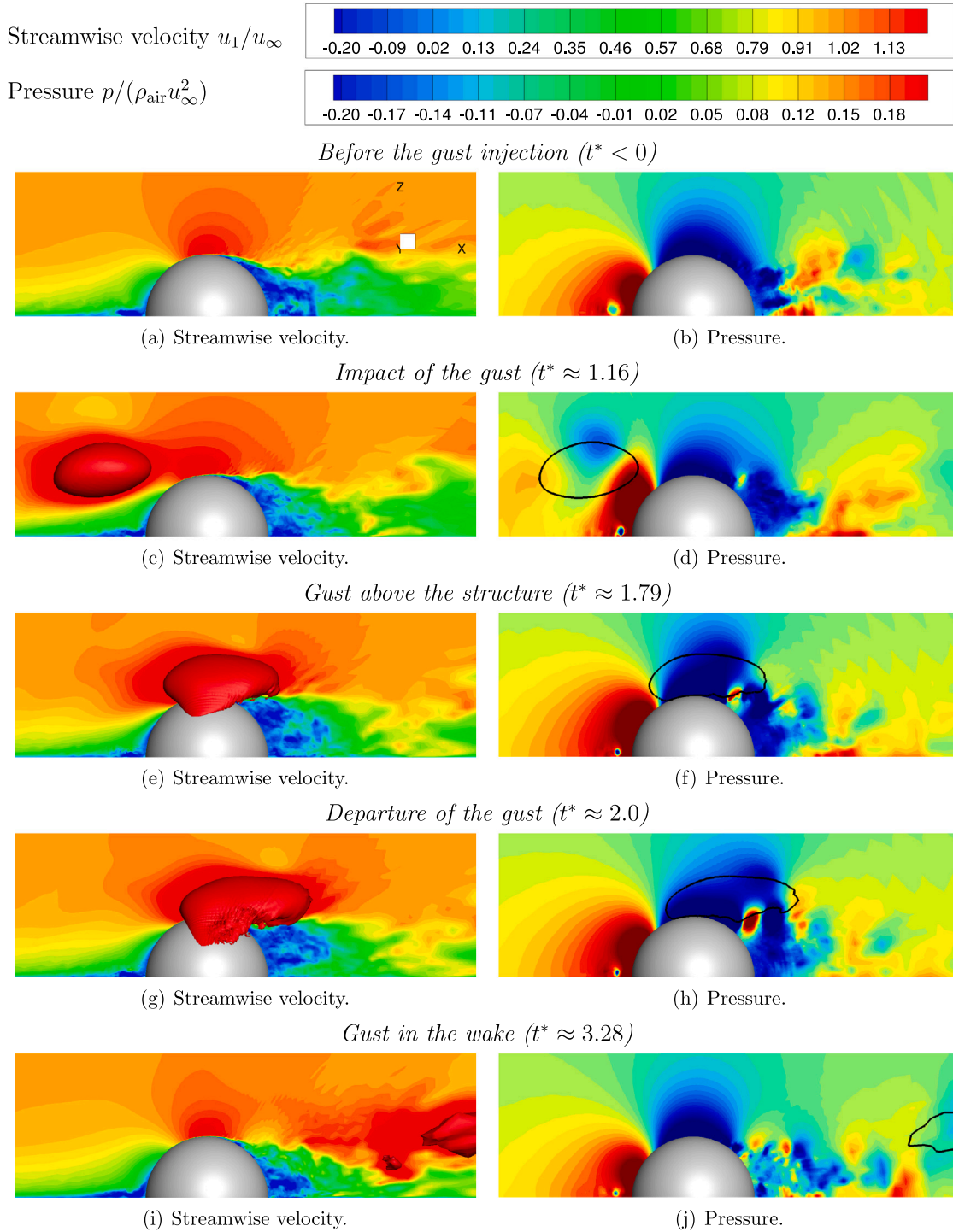


**Fig. 3. Rigid case** ( $z_g^0/D = 4/8$ ,  $A_g/u_\infty = 1.0$ ,  $L_g^z/D = 1.0$ ): Wind gust (shape of an American football in (c)) moving downstream and impacting the rigid hemisphere (Left: streamwise velocity  $u_1/u_\infty$ ; Right: pressure  $p/(\rho_{\text{air}}u_\infty^2)$ ) in a slice in the symmetry plane  $y = 0$ ). The position of the gust structure is highlighted by a red iso-surface of the streamwise velocity  $u_1/u_\infty = 1.4$  for the streamwise velocity and by a black iso-line  $u_1/u_\infty = 1.4$  for the pressure. (For interpretation of the references to color in this figure legend, the reader is referred to the web version of this article.)

streamwise force coefficient during the impact and the vertical force coefficient during the suction on the tip of the hemisphere is expected. The relation can also be derived based on the energy of a continuous time signal, which is defined as the area under the squared magnitude of the considered signal. Inserting the representation of the discrete gust given by Eqs. (1) and (2) into this relation delivers a quadratic dependence on the gust strength  $A_g$ .

For the second peak  $c_x^{\text{max}, D}$  appearing during the departure of the gust, this quadratic relationship is not so obvious anymore. The peak values still strongly increase with increasing  $A_g$ , but especially for the cases, where the gust is located closer to the bottom wall (e.g.,  $z_g^0/D = 2/8$ ), a degressive increase of the peak value  $c_x^{\text{max}, D}$  is observed. This phenomenon can be explained by observing the evolution of the three-dimensional shape of the gust in time as represented by a blue

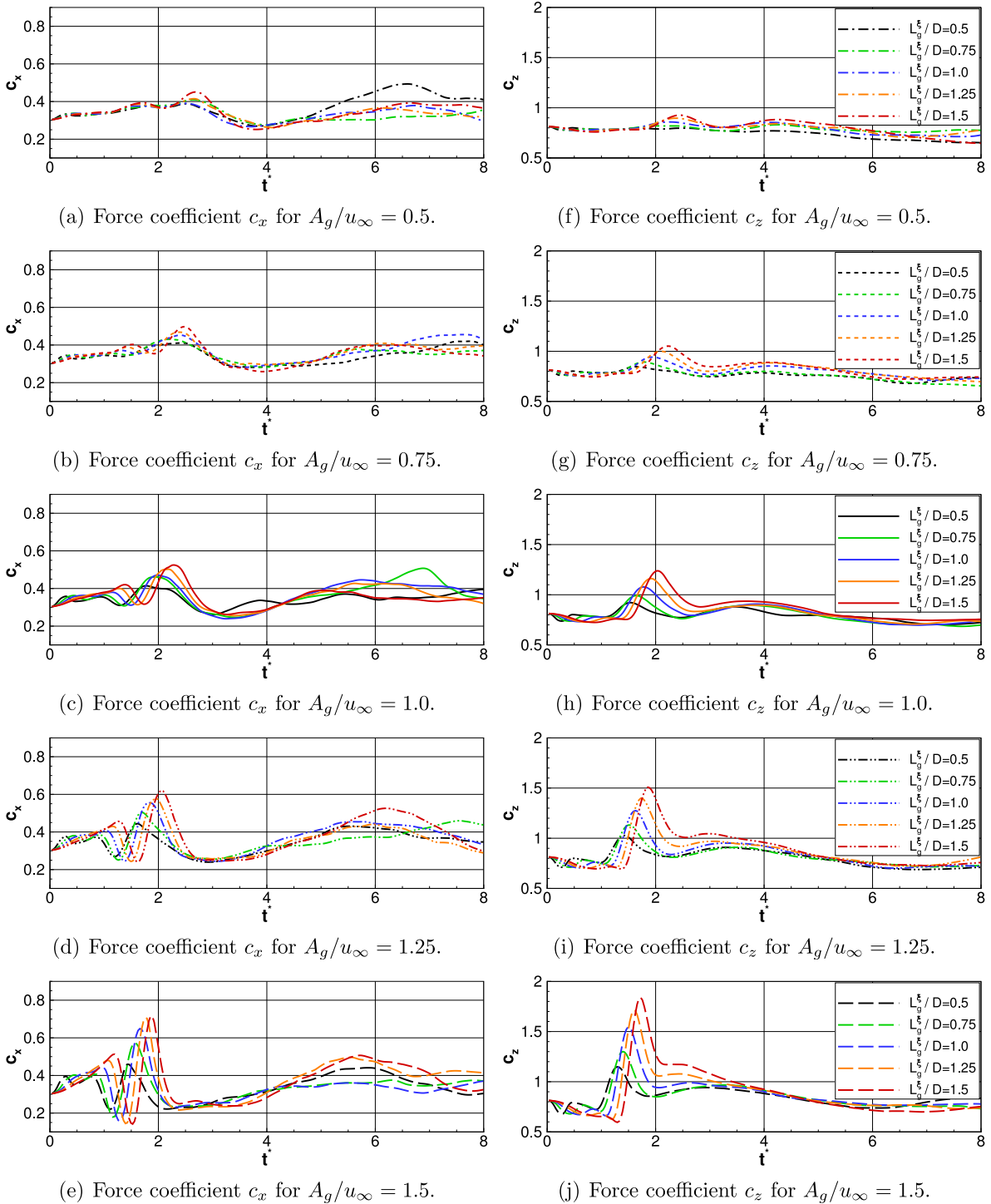


Fig. 4. Rigid case ( $z_g^0/D = 4/8$ ): Streamwise  $c_x$  and vertical  $c_z$  force coefficients predicted for different gust strengths and gust lengths as a function of the dimensionless time  $t^*$ .

iso-surface of the streamwise velocity in Fig. 9. For a gust injection at the height of the hemisphere tip ( $z_g^0/D = 4/8$ ) only the lower part of the gust is affected by the bluff body and therefore the major part of the gust travels over the structure. For the gust injection near the wall ( $z_g^0/D = 2/8$ ) the major part of the gust is deflected by the bluff body after the impact. A part of the gust swerves to the left while another part passes the structure to the right (visible by the iso-surface and also in the increase of the vorticity magnitude near the bottom wall in Fig. 9(h)). Thus, only a limited part of the gust reaches the backside of the hemisphere (see Fig. 9(i)). This leads to decreasing values of  $c_x^{\max, D}$  for decreasing gust heights  $z_g^0$ .

Another interesting observation is that in case of a gust close to the bottom<sup>1</sup> the peak values of the impact event  $c_x^{\max, I}$  are larger than those for the departure  $c_x^{\max, D}$ . However, with larger distances of the gust from the bottom the trends turn around. In this case the peak values during the departure of the gust are much stronger than during the impact. For  $z_g^0/D = 5/8$  the effect can easily be explained. In that case the center of the gust is already above the apex of the

<sup>1</sup> Except for low values of  $A_g$ .

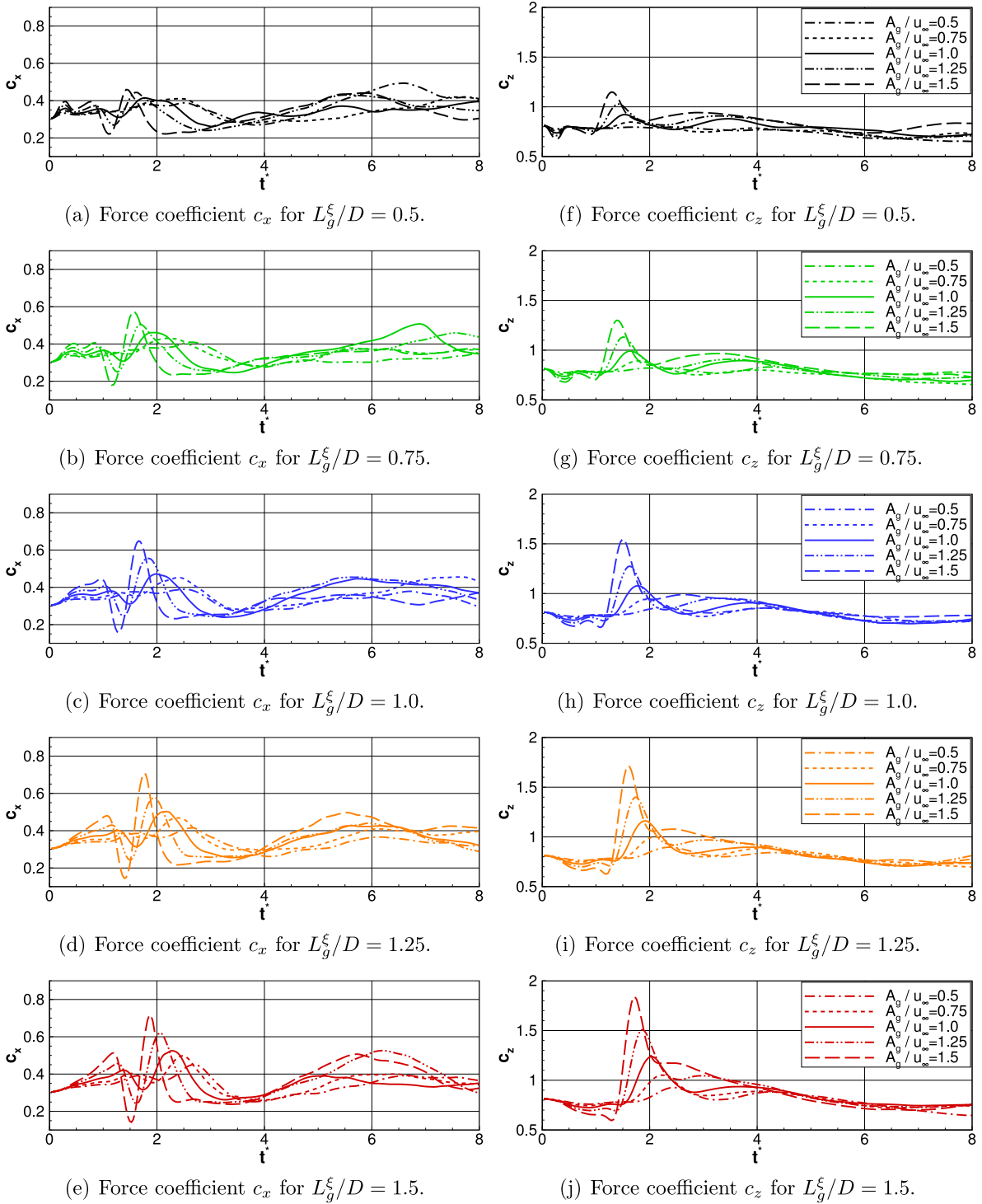


Fig. 5. Rigid case ( $z_g^0/D = 4/8$ ): Streamwise  $c_x$  and vertical  $c_z$  force coefficients predicted for different gust strengths and gust lengths as a function of the dimensionless time  $t^*$ .

hemisphere. Thus, solely the arm of the gust hits the structure directly leading to low values of  $c_x^{\max, I}$ . Nevertheless, the low pressure region in the recirculation area behind the hemisphere leads to large values of  $c_x^{\max, D}$ . An explanation why the peak values of  $c_x^{\max, I}$  are larger than those of  $c_x^{\max, D}$  for low values of  $z_g^0/D$  is provided below.

In the second set of figures (Fig. 7) the maximal force coefficients are depicted as a function of the gust length  $L_g^xi$ . Here different gust amplitudes are represented by different lines, whereas the outcome for different gust heights are again shown in separate sub-figures. Concerning the peak values  $c_x^{\max, I}$  of the streamwise force coefficient

for the impact a more or less linear behavior is visible. Taking again the energy of a continuous time signal into account, a linear dependence is found for a discrete gust of ECG type. Thus, the energy of the gust increases with its length  $L_g^xi$ . Accordingly, the resulting streamwise force rises almost linearly with the gust length. The same applies to the peak values of the vertical force coefficient  $c_z^{\max}$  arising due to the strong suction on the hemisphere when the gust passes over the structure.

The second peak value of the streamwise force coefficient  $c_x^{\max, D}$  shows a deviating behavior. The force still rises with increasing length of the gust as expected due to the linear dependence of the energy

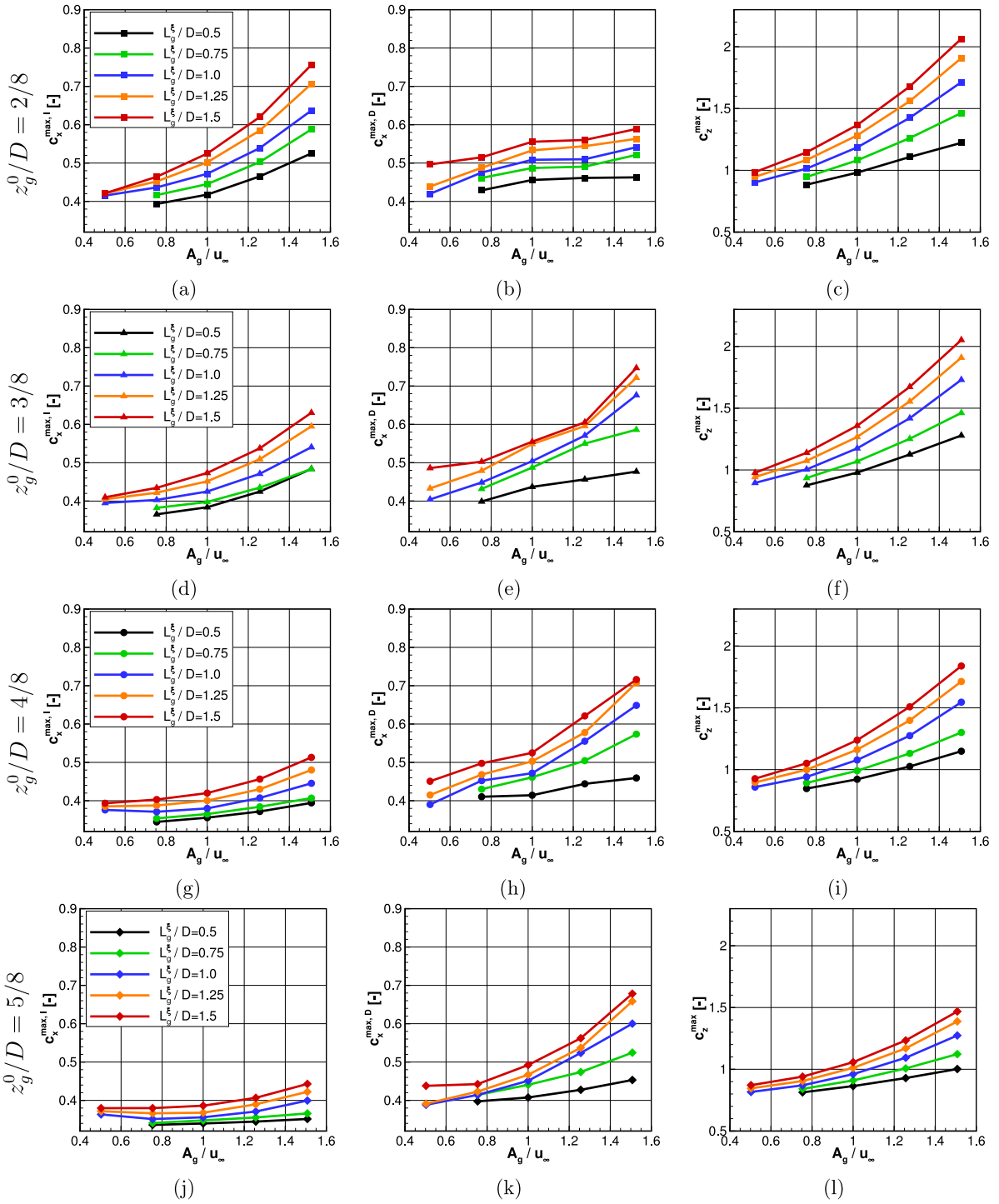


**Fig. 6. Rigid case:** Relations between gust strength  $A_g/u_\infty$  and maximal force coefficients for different gust lengths  $L_g^E/D$  and heights  $z_g^0/D$ . (a), (d), (g) and (j) depict the maximal streamwise force coefficient  $c_x^{max, I}$  during the impact of the gust. (b), (e), (h) and (k) depict the maximal streamwise force coefficient  $c_x^{max, D}$  due to the departure of the gust. (c), (f), (i) and (l) depict the maximal vertical force coefficient  $c_z^{max}$  during the passage of the gust.

of the signal on the length scale. For the lowest value of  $z_g^0/D$  the dependency seems to be approximately linear. However, for higher values, especially in case of  $z_g^0/D = 3/8$  and  $4/8$ , the peak values due to the departure of the gust degressively increase with  $L_g^E$ .

Finally, Fig. 8 shows the results as a function of the height of the gust  $z_g^0$ . The clearest trend is observed for the peak values of the impact event  $c_x^{max, I}$ . For all gust strengths and gust lengths the maxima strongly decrease with an increasing distance from the bottom. When the gust is injected close to the bottom wall, it hits the hemispherical

structure almost in normal direction. For example, at  $z_g^0/D = 2/8$  the inclination is only 30 degree, whereas it rises to 48.6 and 90 degrees in case of  $z_g^0/D = 3/8$  and  $4/8$ , respectively. For the largest value of  $z_g^0/D = 5/8$  the gust only grazes the structure. Consequently, the strong dependence of  $c_x^{max, I}$  is obvious.

The peak values of the vertical force coefficient  $c_z^{max}$  behave differently. For  $z_g^0/D = 2/8$  and  $3/8$  the values are more or less constant. However, for the other two gust heights which represent the cases of the gust injection at the apex of the hemisphere and above, the peak

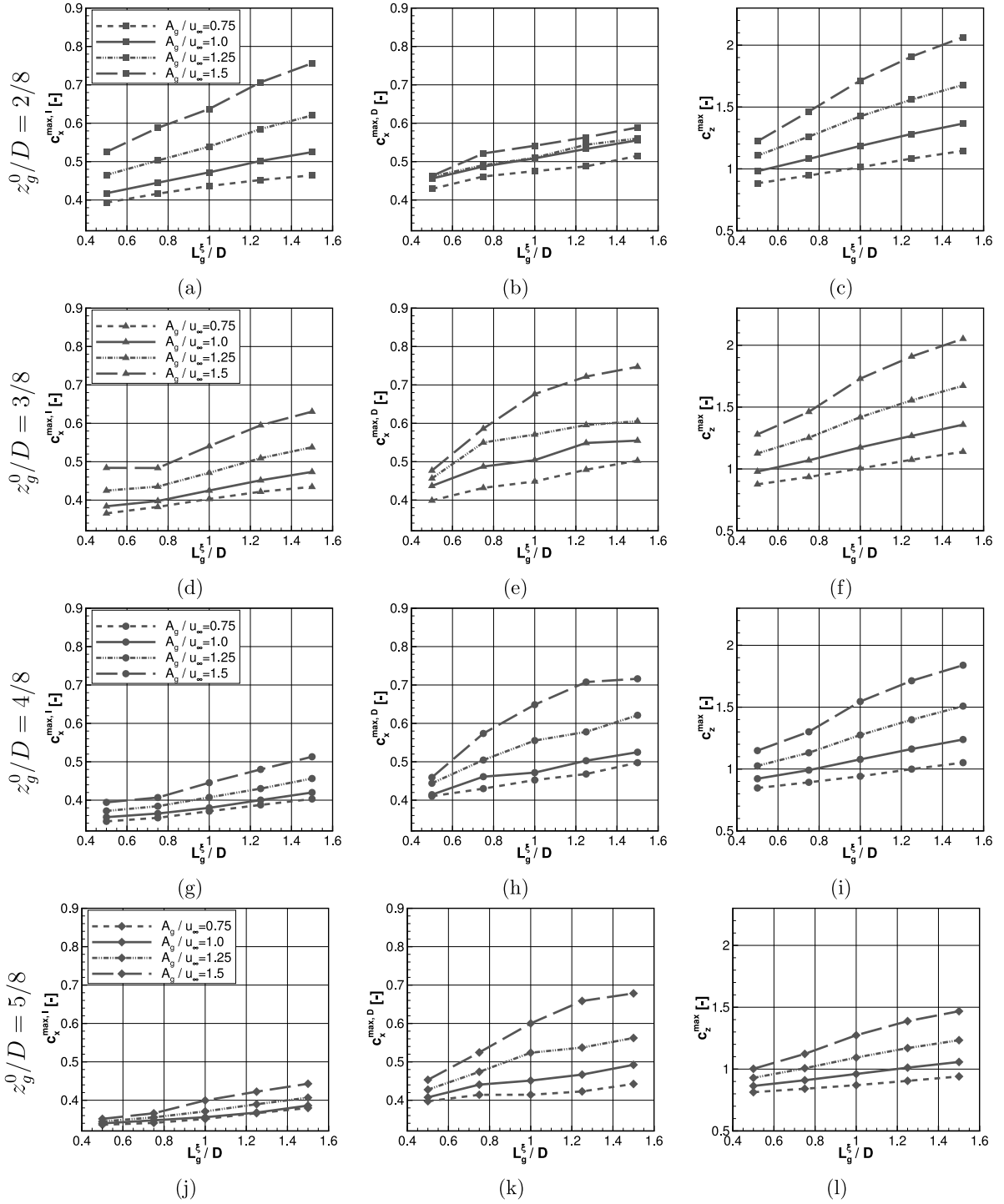


**Fig. 7. Rigid case:** Relations between gust lengths  $L_g^\xi/D$  and maximal force coefficients for different gust strengths  $A_g/u_\infty$  and heights  $z_g^0/D$ . (a), (d), (g) and (j) depict the maximal streamwise force coefficient  $c_x^{\max, I}$  during the impact of the gust. (b), (e), (h) and (k) depict the maximal streamwise force coefficient  $c_x^{\max, D}$  due to the departure of the gust. (c), (f), (i) and (l) depict the maximal vertical force coefficient  $c_z^{\max}$  during the passage of the gust.

values strongly decrease for all gust strengths  $A_g$  and gust lengths  $L_g^\xi$ . At a first glance these results are not expected, since for low values of  $z_g^0/D$  the gust splits and parts travel left and right of the bluff body as demonstrated in Fig. 9(h). Therefore, the suction phenomenon resulting from the gust traveling over the hemisphere should be reduced. Why is the contrary observed? Since the shear stress has only a minor contribution to the force coefficients for this geometry (see De Nayer et al., 2022), Fig. 10 compares the pressure distribution on the bluff body at the time instant, where  $c_z^{\max}$  is reached. Two heights of gust

injection are selected ( $z_g^0/D = 2/8$  and  $z_g^0/D = 4/8$ ). For  $z_g^0/D = 4/8$  the area of low pressure is concentrated on the top as expected since solely the lower part of the gust is blocked by the obstacle in the flow field. The blocking of the flow typically leads to stronger accelerations of the flow and thus stronger suction pressures in the vicinity of the hemisphere. However, in the case  $z_g^0/D = 2/8$  the low pressure area is present on the top but also extends to the left and right sidewalls down to the bottom wall. This leads to a much larger low-pressure zone than for  $z_g^0/D = 4/8$ . Since the magnitudes of the low pressure are similar,

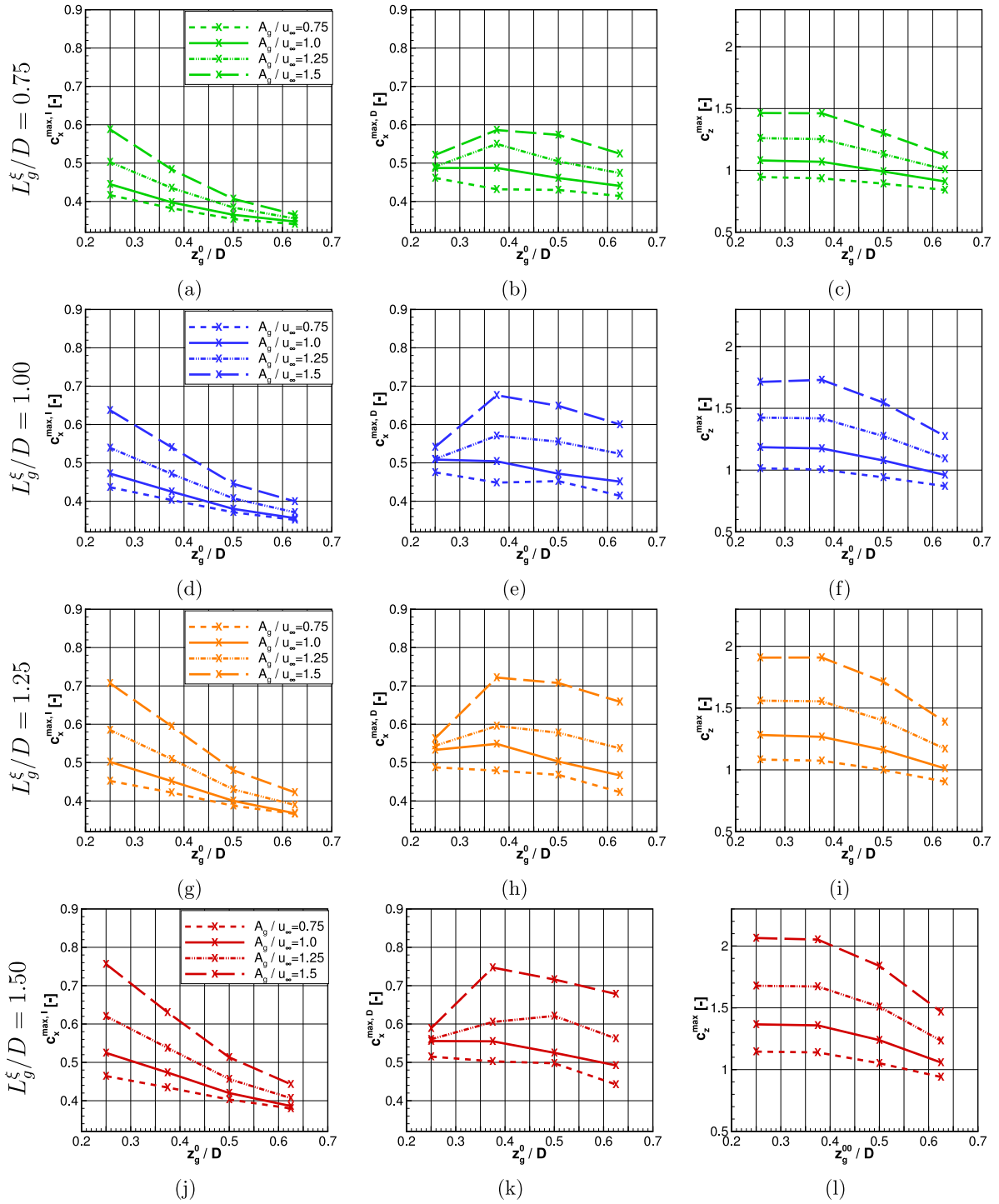


**Fig. 8. Rigid case:** Relations between gust height  $z_g^0/D$  and maximal force coefficients for different gust strengths  $A_g/u_\infty$  and gust lengths  $L_g^\xi/D$ . (a), (d), (g) and (j) depict the maximal streamwise force coefficient  $c_x^{\max, I}$  during the impact of the gust. (b), (e), (h) and (k) depict the maximal streamwise force coefficient  $c_x^{\max, D}$  due to the departure of the gust. (c), (f), (i) and (l) depict the maximal vertical force coefficient  $c_z^{\max}$  during the passage of the gust.

this larger low-pressure area explains the higher  $c_z^{\max}$  for low value of  $z_g^0/D$ .

Again, the distributions of  $c_x^{\max, D}$  show the most complex non-linear behavior. The values first rise with increasing  $z_g^0$ , then stay nearly constant for  $3/8 \leq z_g^0/D \leq 4/8$  and fall again for larger distances of the gust from the bottom. As mentioned before, the gust is only faintly visible in the recirculation area behind the body for the lowest value of  $z_g^0/D = 2/8$  (see Fig. 9(i)). For the opposite case of  $z_g^0/D = 5/8$  the major part of the gust travels over the hemisphere. This explains

the low values of  $c_x^{\max, D}$ . In case of injection heights in the middle, e.g.  $z_g^0/D = 3/8$  or  $z_g^0/D = 4/8$ , the shape of the deformed gust after hitting the structure is similar (see Figs. 9(c) and 9(f)) yielding approximately equal values for  $c_x^{\max, D}$ .

Looking towards the worst-case scenario for the rigid configuration, the investigations on the influence of the parameters  $A_g$ ,  $L_g^\xi$  and  $z_g^0$  on the resulting fluid forces lead to the following conclusions:

- The streamwise force coefficient reaches its maximum  $c_x^{\max, I}$  during the impact of the gust for the smallest injection height

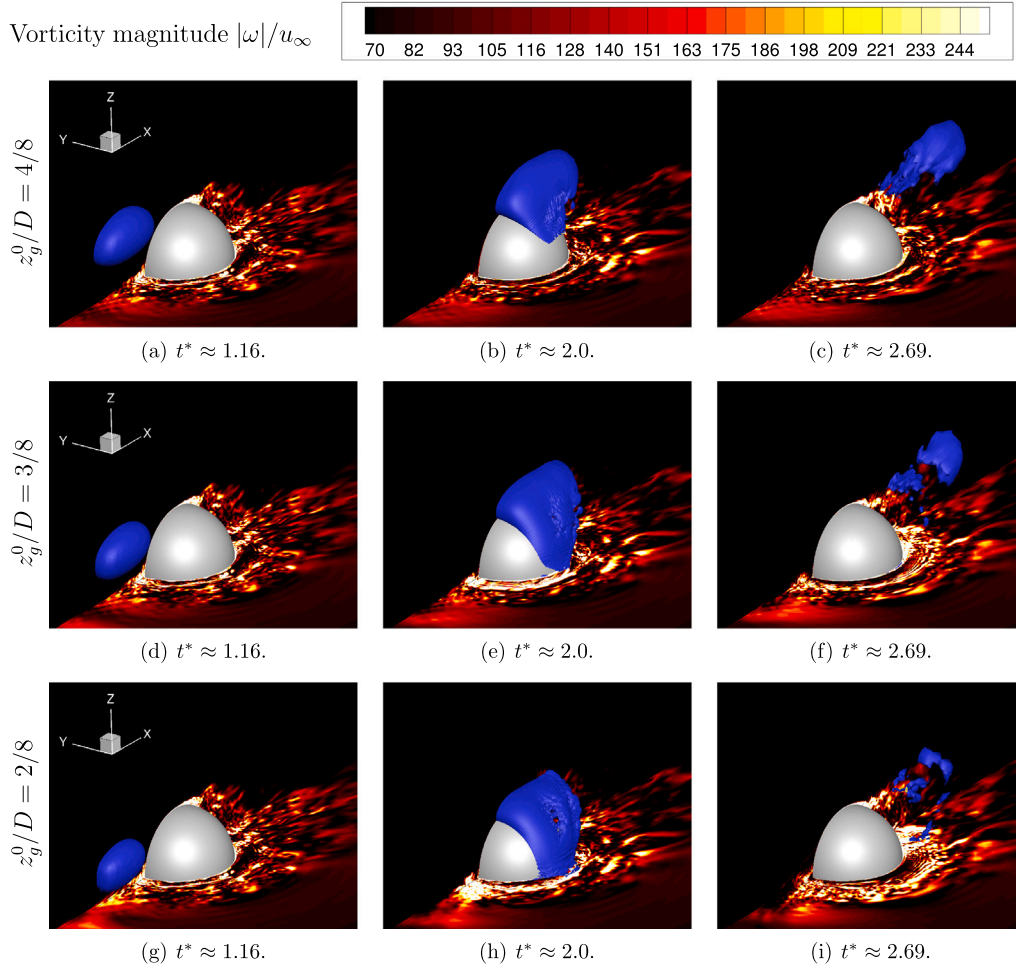


**Fig. 9. Rigid case** ( $A_g/u_\infty = 1.0$ ,  $L_g^\xi/D = 1.0$ ): Comparison of the shape of a wind gust injected at the height  $z_g^0/D = 2/8$ ,  $z_g^0/D = 3/8$  and  $z_g^0/D = 4/8$  for three instants of time. The position of the gust structure is highlighted by a blue iso-surface of the streamwise velocity  $u_1/u_\infty = 1.4$ . The flow field is depicted using the vorticity magnitude  $|\omega|/u_\infty$  in the symmetry plane  $y=0$  and in a plane near the bottom wall. (For interpretation of the references to color in this figure legend, the reader is referred to the web version of this article.)

$z_g^0/D = 2/8$ , the largest gust length  $L_g^\xi/D = 1.5$  and the largest gust strength  $A_g/u_\infty = 1.5$ .

- The second maximum of the streamwise force coefficient  $c_x^{\max, D}$  due to the departure of the gust from the body is obtained for medium values of the injection height  $z_g^0/D = \{3/8, 4/8\}$ , the largest gust length  $L_g^\xi/D = 1.5$  and the largest gust strength  $A_g/u_\infty = 1.5$ .
- The maximum of the vertical force coefficient  $c_z^{\max}$  is found for lower values of the injection height  $z_g^0/D = \{2/8, 3/8\}$ , the largest gust length  $L_g^\xi/D = 1.5$  and the largest gust strength  $A_g/u_\infty = 1.5$ .
- Interesting is that the largest value of  $c_x^{\max, I}$  is very similar to the one of  $c_x^{\max, D}$ , but obtained for different injection heights  $z_g^0/D$ .

#### 4.2. FSI case

The simulations of the flow around the rigid structure under wind gust load are computationally cheap in comparison to the fully coupled FSI case. Although the exact factor varies from case to case, as a rough rule of thumb one can assume that the computational effort for the FSI simulations is about two to three times higher in the present case. That is the main motivation to examine the influence of various gust parameters in the precursor study based on the rigid case as a physical meta-model.

One has learned from this lesson that looking for the worst-case scenario it makes little sense to investigate low gust strength  $A_g$ , which

of course is not astonishing. The second not so obvious insight is that there is no need to study short gust lengths  $L_g^\xi$ . Indeed, the energy of the gust depends on its length. However, short gust lengths lead to stronger slopes in the gust velocity. Thus, the influence of the gust length was not so clear in advance, which is also reflected by the non-linear distributions found for  $c_x^{\max, D}$  and  $c_z^{\max}$ . Note that the statement on the effect of  $L_g^\xi$  is based on the physical meta-model of the rigid structure. To prove that it is also valid for the elastic structure, additional FSI simulations for shorter gust lengths (not described here) are carried out confirming the hypothesis that the statement derived from the meta-model can be transferred to the real structure.

Concerning the gust height  $z_g^0$ , there is no need to run any FSI simulations for  $z_g^0/D \geq 5/8$ , since low values of all three force coefficients are found in the rigid case. Although the results for the rigid case cannot be transferred one-to-one to the flexible case, they still give a clear orientation over the relevant parameter range, which should cover the highest values of  $A_g$  and  $L_g^\xi$  the structure can withstand.

Preliminary coupled simulations for the extreme case of  $A_g/u_\infty = 1.5$  and  $L_g^\xi/D = 1.5$  revealed extremely large deflections of the membrane (see Fig. 11), which could finally not be handled until the end by the present partitioned simulation framework. Furthermore, the associated principal strains occurring in the structure exceed the value of 10% for all three gust injection heights (up to 18% for  $z_g^0/D = 2/8$ ) and thus overshoot the classical limit of 5% for the application of the St. Venant-Kirchhoff material model. Consequently, the gust parameters

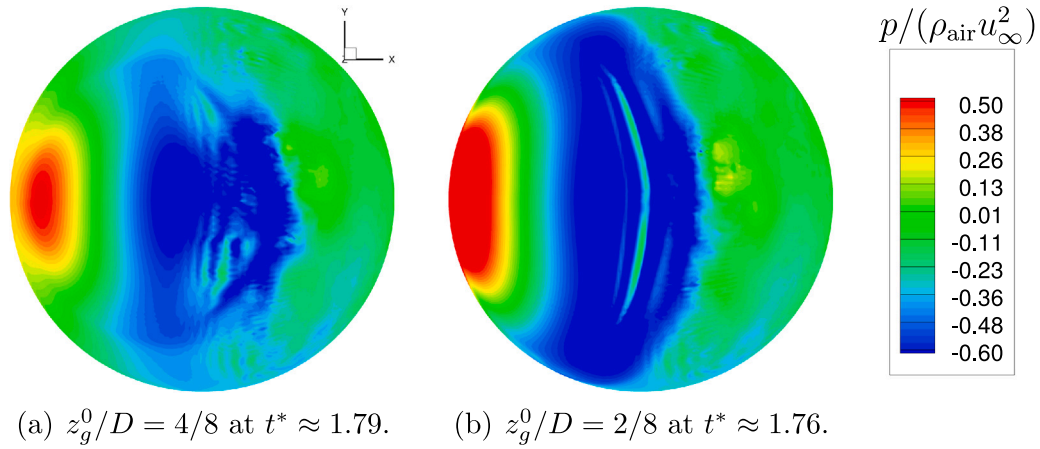


**Fig. 10. Rigid case** ( $A_g/u_\infty = 1.0$ ,  $L_g^e/D = 1.0$ ): Comparison of instantaneous pressure distribution  $p/(\rho_{\text{air}}u_\infty^2)$  on the bluff body for a wind gust injected at the height  $z_g^0/D = 2/8$  with one injected at  $z_g^0/D = 4/8$  for the time instant, where  $c_z^{\text{max}}$  is reached.

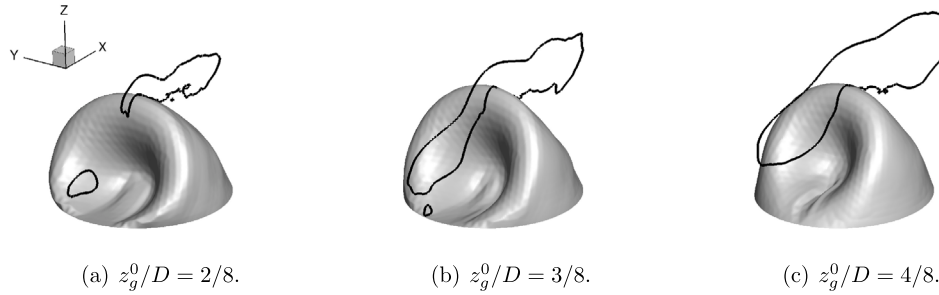


**Fig. 11. Different gust injection heights on flexible case** ( $A_g/u_\infty = 1.5$ ,  $L_g^e/D = 1.5$ ): Deflected membranes just before the simulations stopped ( $t^* \approx 1.99$ ). The gust position is highlighted by a black iso-line of the streamwise velocity  $u_1/u_\infty = 1.4$ .

have to be reduced to  $A_g/u_\infty = 1.0$  and  $L_g^e/D = 1.0$  guaranteeing a stable solution procedure while the deformation of the structure is still very large as will be shown below. Regarding the effect of the height of the gust observed for the rigid case, this parameter should be varied in the range  $2/8 \leq z_g^0 \leq 4/8$ .

For the present FSI investigations (and contrary to the investigations with the rigid structure) the coupled simulations are carried out applying a turbulent boundary layer, which superimposes a constant 1/7 power law with turbulent fluctuations (see Section 2.2). The motivation for this choice is to mimic the incoming atmospheric boundary layer and thus consider a FSI problem close to reality.

#### 4.2.1. FSI physics of the wall-mounted flexible structure

The FSI physics including the flow field and the structural deflections occurring during a gust impact on a wall-mounted flexible hemispherical structure were recently described in detail in De Nayer et al. (2022). Thus, here solely the important points are repeated.

Undergoing a quasi-static load generated by the incoming turbulent boundary layer the membranous structure is already slightly deformed at the front before the gust enters the domain. Due to the impact of the gust the front of the membrane grows hollow and a zone of high pressure appears at this place (see Fig. 13). The maximum of the deflection in this indentation at the front is reached with a certain delay compared to the time, where the maximum of the total fluid forces is attained. The increase of  $c_z$  due to the traveling of the gust over the structure induces a vertical deflection of the tip of the membrane. After the departure of the gust the structure tends to recover to its original slightly deformed state. An oscillation of the indentation at the front against the streamwise direction is observed.

#### 4.2.2. Influence of the gust height $z_g^0$ on the FSI phenomena

In order to investigate the effect of the gust height  $z_g^0$  on the resulting FSI phenomena, the flow field around the deflected structure is at first studied based on the fluid force coefficients and the pressure distribution at different time instants. In a second step, the inner strains and the von Mises stresses occurring in the membrane are examined.

The fluid force coefficients in streamwise and vertical directions predicted for three gust injection heights are shown in Fig. 12(c). Similar to the rigid case two peaks ( $c_x^{\text{max, I}}$  and  $c_x^{\text{max, D}}$ ) are present for the streamwise force coefficient. One maximum  $c_z^{\text{max}}$  appears for the vertical force. The magnitude of the peaks  $c_x^{\text{max, I}}$  and  $c_x^{\text{max, D}}$  increases for decreasing  $z_g^0$ . The  $c_x^{\text{max, I}}$  values are lower than for the rigid case. Obviously, the deviations of the membrane from the hemispherical shape reduce the drag force. The observation on  $c_x^{\text{max, D}}$  differs from the results predicted for the rigid model (see Fig. 8(e)), where a maximum is reached for medium values of  $z_g^0$ . The time interval between both maxima obtained for the membrane reduces for decreasing  $z_g^0$  values, i.e.,  $c_x^{\text{max, I}}$  occurs later and  $c_x^{\text{max, D}}$  earlier (see Fig. 12(c)). By decreasing  $z_g^0/D$  the predictions with the membranous model do not show the continuous increase of the vertical force coefficient and the plateau observed in the rigid case (see Fig. 8(f)). Instead, the maximum appears for  $z_g^0/D = 3/8$ . Nevertheless, it can be noticed that the lift forces for all gust injection heights are higher than in the rigid case.

The pressure distributions in the symmetry plane  $y = 0$  and near the wall are chosen to describe the flow field in Fig. 13, since the pressure is the major contribution to the fluid forces acting on the structure. Figs. 13(a), (c) and (e) represent the system at  $t^* = 1.0$ , i.e., the end of the gust injection. After its release, the gust freely travels downstream. Since the injection zone is located close to the structure, the gust touches the front of the body at about  $t^* = 1.0$ . For a low injection height of  $z_g^0/D = 2/8$ , the presence of the bluff body results

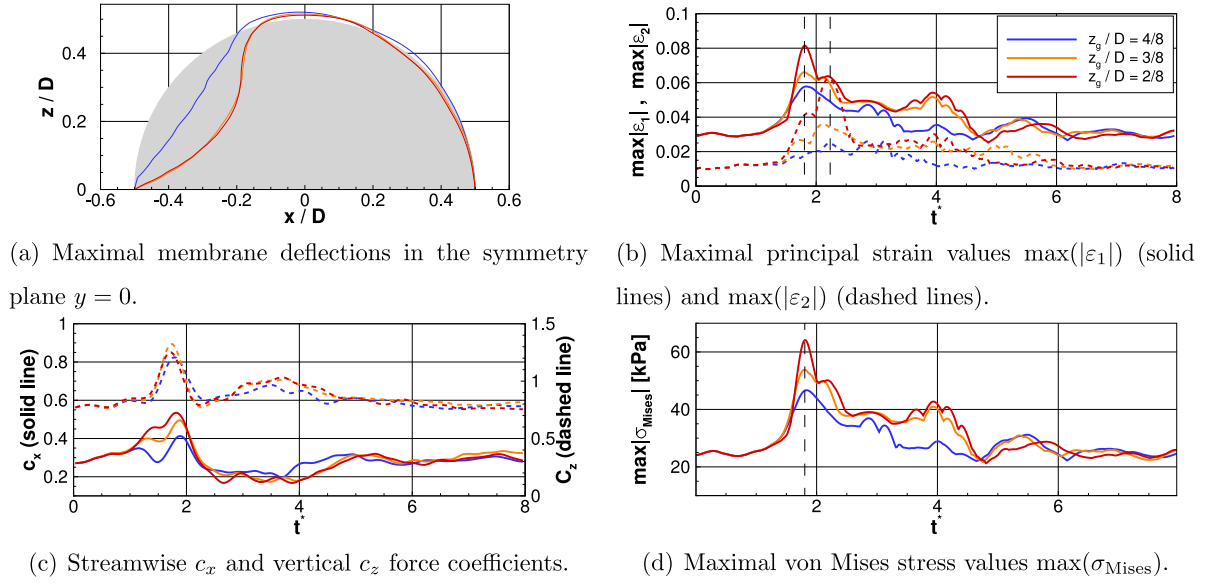


Fig. 12. Different gust injection heights on flexible case ( $A_g/u_\infty = 1.0$ ,  $L_g^e/D = 1.0$ ).

in a blocking of the flow. As a consequence the shape of the gust is already slightly deformed at  $t^* = 1.0$  as visible by the black iso-line in Fig. 13(e). The pressure distributions on the sides and in the wake remain more or less identical for the three investigated gust heights. The flexible structure is already slightly deflected at the front. This is due to the quasi-static load resulting from the incoming turbulent boundary layer. The parameter  $z_g^0/D$  has no influence on this deflection for  $t^* < 1$ .

Major changes of the flow field are expected for the largest distortion of the structural shape. The problem is fully three-dimensional. Nevertheless, the tracking of the maximal deflection is reduced to the symmetry plane  $y = 0$ . In order to quantify this deflection by one value per time step, the difference between the deformed  $\mathbf{r}_{def}$  and undeformed shape  $\mathbf{r}_{ref}$  is built and the  $L_2$ -norm is applied, i.e.,  $\Delta r = \|\mathbf{r}_{def} - \mathbf{r}_{ref}\|_2$ . This deflection value  $\Delta r$  is computed at each time step for the three FSI simulations investigated. Then, for each FSI case, the time step is selected, where the deflection value is the largest. For the gust injection height  $z_g^0/D = 4/8$ , the maximal deflection is reached at  $t^* \approx 2.30$  depicted in Fig. 13(b). By decreasing  $z_g^0/D$  the time, when the structure is maximally deflected, increases ( $t^* \approx 2.54$  for  $z_g^0/D = 3/8$  depicted in Fig. 13(d),  $t^* \approx 2.56$  for  $z_g^0/D = 2/8$  depicted in Fig. 13(f)). In addition, by decreasing the height  $z_g^0/D$ , the maximal deflection increases. This observation is expected, since for low values of  $z_g^0/D$  a larger part of the gust hits the body. However, the increase has an upper limit as visible in Fig. 12(a), where the maximal deflections in the symmetry plane are found to be quasi identical for  $z_g^0/D = 2/8$  and  $3/8$ . By decreasing  $z_g^0/D$ , the pressure distribution reveals a larger and stronger high-pressure area at the indentation on the front. In parallel, a small region of low pressure located just before the high pressure area becomes more intensive. It corresponds to the strengthened horseshoe vortex induced by the strong indentation of the membrane at this instant in time.

Now focusing on the deformation of the membranous structure, the maximal inner strains are traced in space and time. The principal strains  $\epsilon_1$  and  $\epsilon_2$  are computed relying on the components of the Green-Lagrange strain tensor defined over the surface of each finite element. The maxima over the whole shape of each principal strain  $\max(|\epsilon_1|)$  and  $\max(|\epsilon_2|)$  are calculated at each time instant and depicted in Fig. 12(b). The global maxima of both principal strains (i.e., the time instants at which the membrane elements are the most deformed in each of the principal directions) do not occur at the same time and are not coincident with the maximum deflection of the shape (i.e., the

time instant at which the displacements of the nodes are the largest). A peak in the evolution of  $\max(|\epsilon_1|)$  is visible around  $t^* \approx 1.8$  for the three different gust injection heights. Shortly later another peak is observed in  $\max(|\epsilon_2|)$  around  $t^* \approx 2.2$ . The maximum deflection is reached at  $t^* \approx 2.5$  a little bit later.

The inner stress is of major interest for the worst-case scenario since the material fails beyond a certain inner stress limit. For the current FSI investigation the von Mises stress  $\sigma_{Mises}$  is chosen. The maximum of  $\sigma_{Mises}$  at each time step is shown in Fig. 12(d). The temporal evolution of  $\max(\sigma_{Mises})$  closely follows  $\max(|\epsilon_1|)$ , since the magnitude of  $\epsilon_1$  is significantly larger than  $\epsilon_2$ . It is obvious that the gust injection height  $z_g^0$  has a major influence on the maximum value of  $\sigma_{Mises}$ . Decreasing the injection height leads to higher inner stresses. The maximum inner stress generated by the quasi-static load due to the background turbulence is around 25 kPa. The impact of a gust injected at  $z_g^0/D = 4/8$  leads to an increase of this maximal inner stress up to 47 kPa, i.e., about twice of the quasi-static load. Reducing the injection height to  $z_g^0/D = 2/8$  a gust of the same strength generates a maximal inner stress of 64 kPa, i.e., about 2.5 times higher than the quasi-static load.

Fig. 14 depicts the evolution of the  $\sigma_{Mises}$  distribution for the three remarkable instants in time (global maximum of  $\epsilon_1$ , global maximum of  $\epsilon_2$ , maximum deflection) for  $z_g^0/D = \{2/8, 3/8, 4/8\}$ . Interestingly, the magnitude of  $\sigma_{Mises}$  inside the indentation of the structure is not as high as expected except for the case  $z_g^0 = 2/8$ . In this case the maximum is found in the indentation near the bottom wall at  $t^* \approx 1.8$  (when  $\epsilon_1$  is maximum). It is a direct consequence of the gust injection at a low height. The membrane elements at the front near the bottom wall are fixed to the bottom wall but have to expand undergoing the strong gust load leading to large inner stresses in this area. In addition high values of  $\sigma_{Mises}$  are found on the top and around this indentation for all values of  $z_g^0$ . This area of high structural stresses can be linked with the suction induced by the low pressure of the fluid as represented in Fig. 15. Moreover, for the three  $z_g^0$  investigated the maximum inner stress is not predicted at the strongest deflection of the shape. The  $\sigma_{Mises}$  distributions corresponding to the most deflected structure (around  $t^* \approx 2.5$ ) are shown in Figs. 14(c), (f) and (i). At this instant in time the strongest inner stresses are located near the apex of the structure, but their magnitudes are much lower than those reached before (at  $t^* \approx 1.8$ ). The large indentation at the front only includes low inner stress values meaning that the deformation of the structural elements is limited in this area.

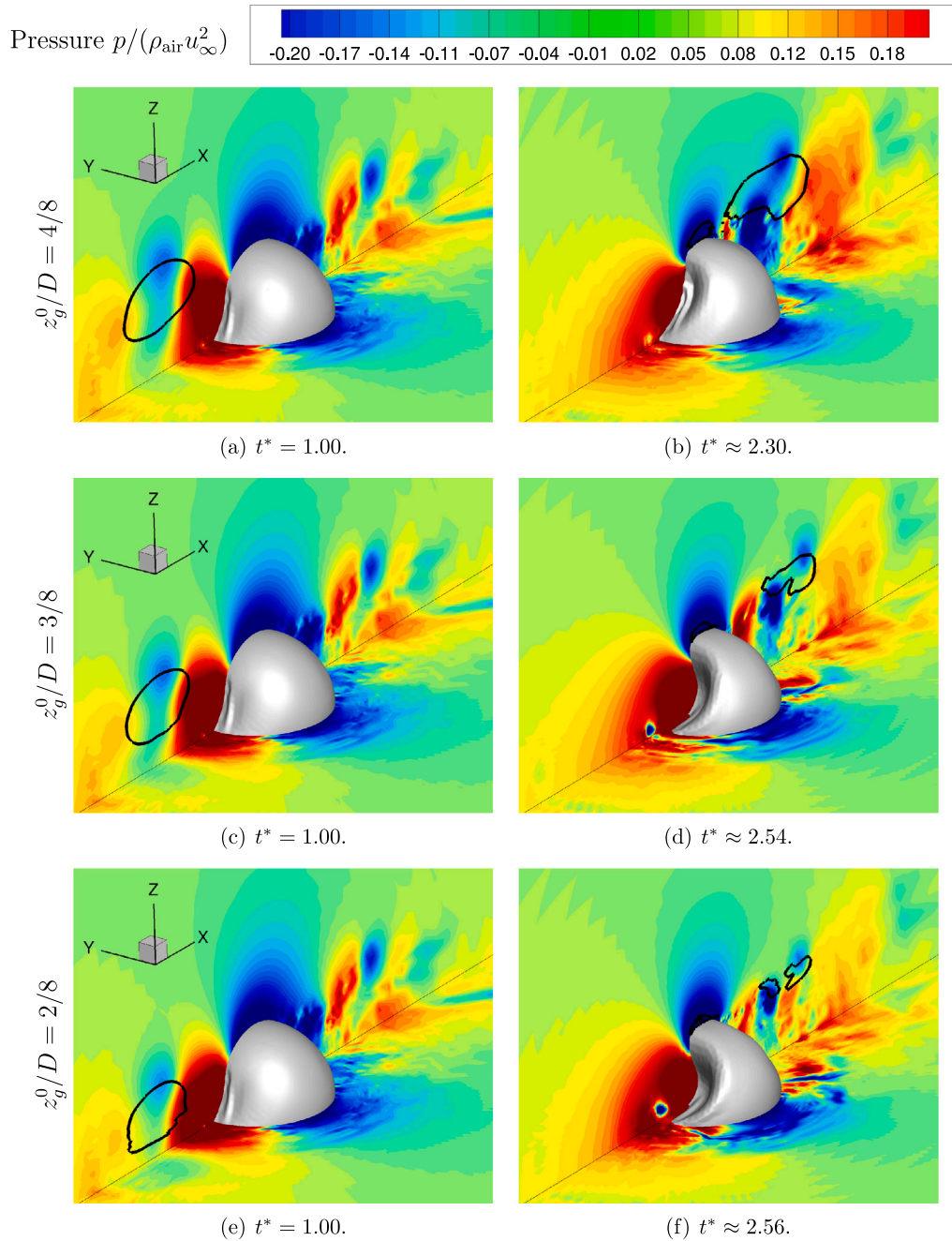


**Fig. 13.** Different gust injection heights on flexible case ( $A_g/u_\infty = 1.0$ ,  $L_g^z/D = 1.0$ ): Comparison of the deflected membranous structure for wind gusts injected at  $z_g^0/D = \{2/8, 3/8, 4/8\}$  (pressure  $p/(\rho_{\text{air}} u_\infty^2)$ ) in a slice near the bottom wall and in the symmetry plane  $y = 0$ . The pictures on the left correspond to the end of the gust injection. Those on the right are associated with the maximal deflections of the structure. The gust position is highlighted by a black iso-line of the streamwise velocity  $u_1/u_\infty = 1.4$  in the symmetry plane.

Looking towards the worst-case scenario for the flexible case, the gust injection height  $z_g^0/D$  plays a central role on the maximum of the streamwise fluid force, on the maximal deflection and on the maximum of the inner stress occurring in the material.

#### 4.2.3. Effect of the superposition of the gust with background turbulence

Wind gusts typically appear in the atmospheric boundary layer. Thus, the classical gust structure given for example by the ECG type in Eq. (2) has to be superimposed by the background turbulence of the boundary layer. This superposition can have different effects. On the one hand, the turbulent fluctuations can augment the effect of the gust or on the other hand, a partial cancellation may take place. This depends on how the two contributions coincide. Consequently,

the effect of the superposition is difficult to estimate in advance, especially since the flow field of the turbulent boundary layer is three-dimensional and instantaneous. In order to get an estimate on the effect of the background turbulence, a series of 25 coupled FSI simulations is carried out. The gust parameters chosen for the present investigation correspond exactly to those in Section 4.2.2, i.e.,  $A_g/u_\infty = 1$ ,  $L_g^z/D = 1$  and  $z_g/D = 4/8$ . The resulting gust is strong enough to be clearly distinguished from the turbulent fluctuations of the background flow and leads to significant but predictable deformations of the membrane. In the reference simulation (denoted FSI 0) the gust is injected directly after the restart, which continues the preceding simulation with continuous turbulent inflow fluctuations. In the other simulations (I to XXIV) again the same restart file for the fluid flow and the structure as well

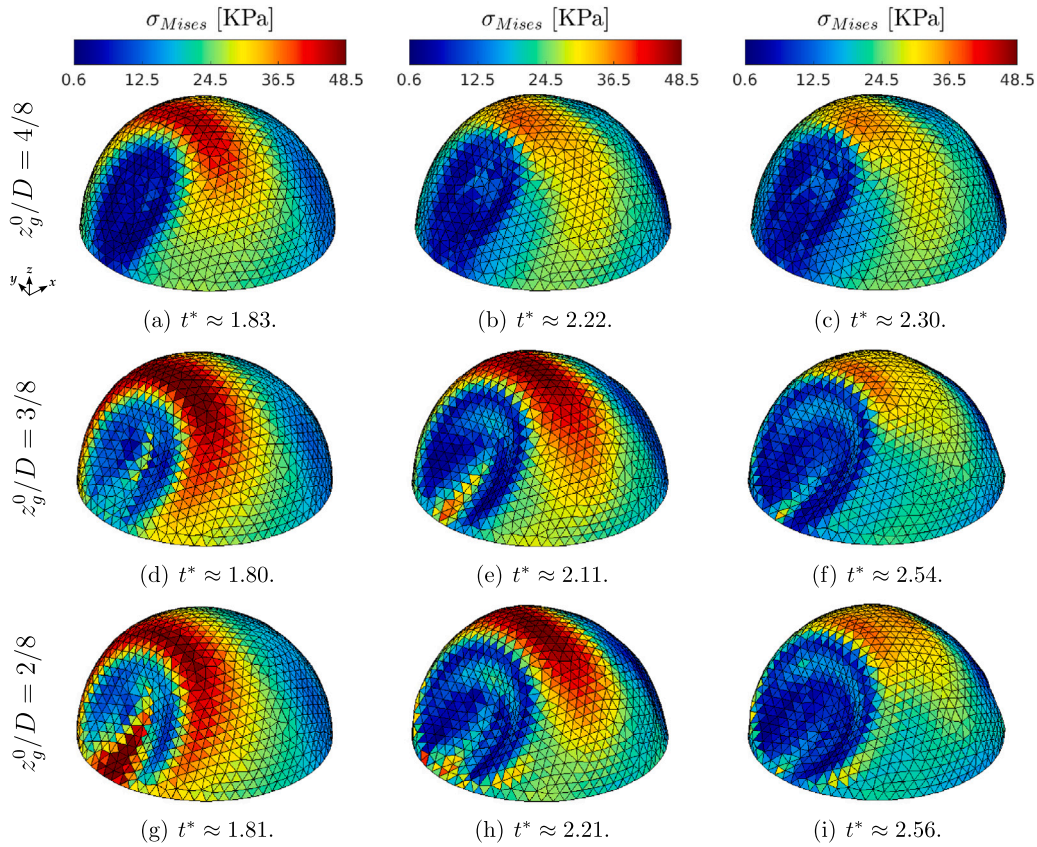


Fig. 14. Different gust injection heights on flexible case ( $A_g/u_\infty = 1.0$ ,  $L_g^z/D = 1.0$ ): Distribution of the von Mises stresses for the time instant at which  $\max(|\epsilon_1|)$  and thus also  $\max(\sigma_{Mises})$  is maximum ((a), (d), (g)), for the time instant at which  $\max(|\epsilon_2|)$  is maximum ((b), (e), (h)) and for the maximal deflection ((c), (f), (i)).

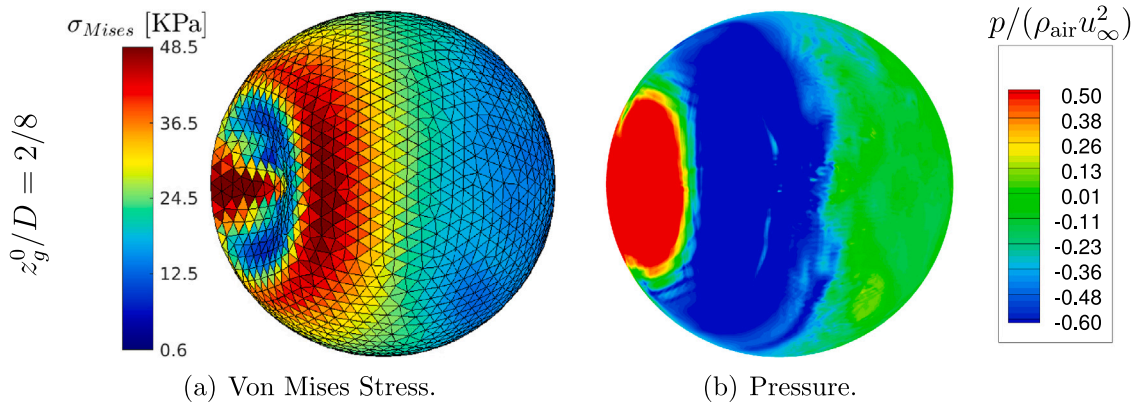


Fig. 15. Comparison of the instantaneous von Mises stress  $\sigma_{Mises}$  with the pressure  $p/(\rho_{air}u_\infty^2)$  on flexible case ( $A_g/u_\infty = 1.0$ ,  $L_g^z/D = 1.0$ ): Wind gust injected at the height  $z_g^0/D = 2/8$  and the time instant  $t^* \approx 1.81$ , at which  $\sigma_{Mises}$  is maximum.

as the turbulent inflow data are used. Thus, the initial conditions are identical to the reference simulation. The only difference is that the gusts are injected with a certain dimensionless time delay of  $\Delta t_{delay}^* = 1, 2, 3$  until 24 compared to the gust injection time of FSI 0, respectively. These 24 configurations are denoted according to the time delay in Roman numerals. Consequently, the same gust is superimposed on 25 different background flows allowing to evaluate the variation of the resulting forces, deflections and von Mises stresses as a result of these superpositions.

The predicted streamwise and vertical force coefficients are compared in Fig. 16. Note that for the sake of a direct comparison the time axes for FSI I to XXIV are accordingly shifted to fit the time of the reference simulation. Obviously, the time histories of the force

coefficients  $c_x$  and  $c_z$  obtained for the 25 cases differ in terms of the absolute values. Visible deviations can also be observed for the peak values, which are of great importance for the worst-case scenario. For example, the peak value of  $c_z$  varies between 1.15 (FSI XIV) and 1.32 (FSI III), which is about 14% with respect to the mean value and thus not negligible. Variations of the same order of magnitude are visible for the streamwise force coefficient  $c_x$ . However, evaluating the differences between the local minima and the local maxima in the intervals (a) to (c), the deviations are even stronger between  $\Delta c_x = 0.13$  for FSI XIV and 0.21 for FSI IX.

In order to quantify these variations, some statistics of the force coefficients are computed. Figs. 16(c) and (d) display the time histories of the force coefficients averaged over the 25 simulations including

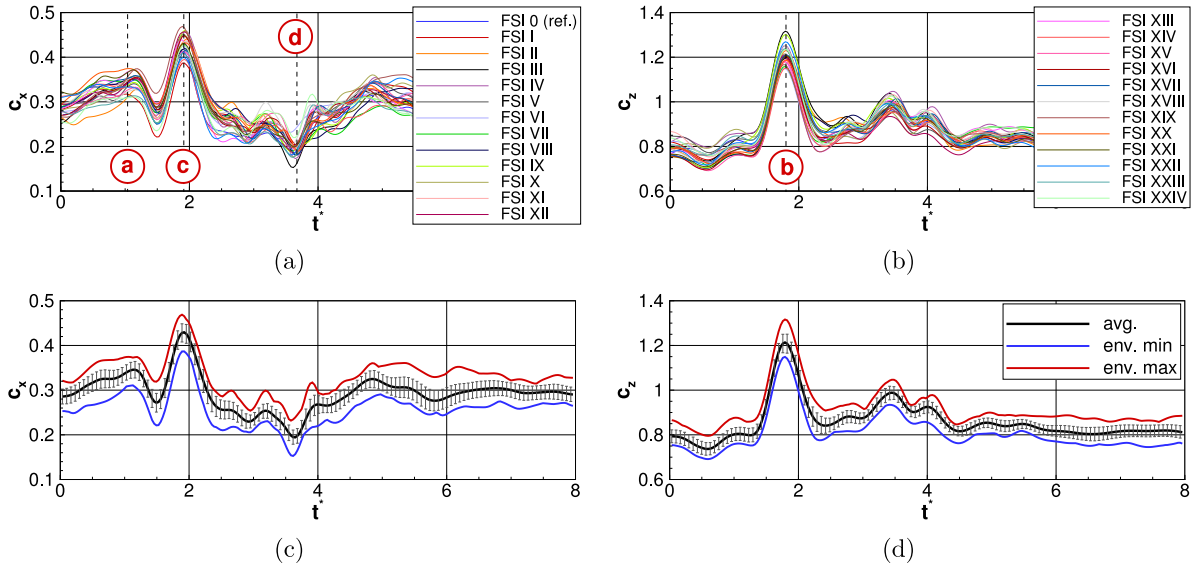


**Fig. 16.** Background turbulence effect on flexible case ( $z_g^0/D = 4/8$ ,  $A_g/u_\infty = 1.0$ ,  $L_g^z/D = 1.0$ ): Streamwise and vertical force coefficients obtained with gusts injected at different time instants. (a)–(b): Results obtained by 25 simulations. (c)–(d): Averaged values of  $c_x$  and  $c_z$  including their envelope and corrected standard deviations.

the envelope and the corrected sample standard deviations.<sup>2</sup> In case of  $c_x$  the associated standard deviation is about 4.9% of the mean value. However, the values provided by the envelope indicate deviations from the mean value corresponding to +9.2% and –9.9% for the maximum and minimum, respectively. Thus, the maximally expected fluctuations are perceptibly larger than those predicted by the standard deviation. Concerning  $c_z$  the maximum value of the standard deviation is 3.6% of the mean value. Again, the deviations provided by the envelope are with +8.5% for the maximum and –5.3% for the minimum about a factor of 2 to 3 larger than the standard deviation. According to a normal distribution it means that between 95% and 99.7% of the values are found in this interval.

The effect of the background turbulence on the response of the flexible membrane is also of high interest. Analog to Section 4.2.2 the deflection value  $\Delta \mathbf{r} = \|\mathbf{r}_{\text{def}} - \mathbf{r}_{\text{ref}}\|_2$  is computed at each time step for all 25 FSI simulations. Then, for each case, the time step is selected, where the deflection value is the largest. The 25 maximally deformed 2D-shapes are compared in Fig. 17(a). As before, statistics are built. The curve obtained by averaging the 25 maximal deformed 2D-shapes is presented in Fig. 17(b) with its envelope and the standard deviations. Substantial differences can be seen in the indentation on the front of the structure. In this area the standard deviations of the dimensionless  $x/D$ - and  $z/D$ -positions reach their maxima. The values provided by the envelope at the point, where the standard deviations are maximal, indicate variations from the mean value ( $\Delta x/D$ ,  $\Delta z/D$ ) corresponding to (+6.5%, +4.7%) for the maximum and (–4.1%, –3.1%) for the minimum. Contrary to the front of the hemispherical structure the background turbulence has only a limited effect on the deflections occurring at the top. The envelope is very close to the averaged deflection in this area. On the rear side, the background turbulence has again a stronger effect on the maximal shape deflection. However, the standard deviations of  $x/D$  and  $z/D$  are at least a factor of two smaller than those on the front.

Last but not least, the influence of the background turbulence on the inner stress occurring in the structure is investigated. For every FSI simulation the maximal von Mises stress predicted at each time step is shown over the dimensionless time in Fig. 18(a). The corresponding averaged curve, its envelope and the associated standard deviations

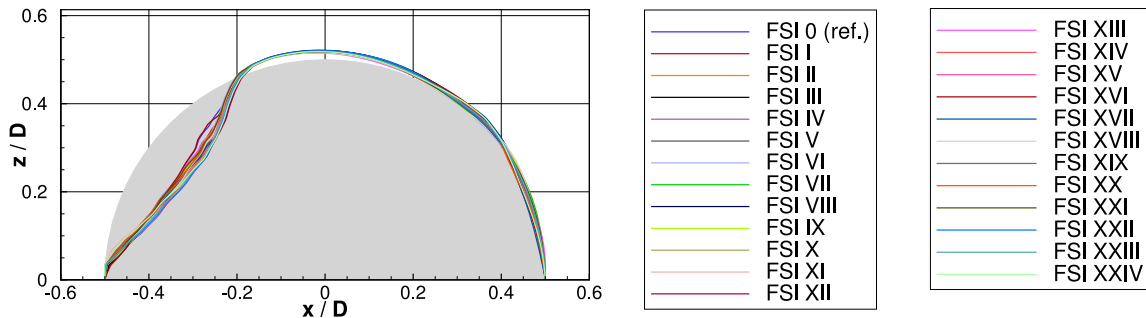
are presented in Fig. 18(b). Assuming that the material fails beyond a certain inner stress limit, only the global maximal value of  $\max(\sigma_{\text{Mises}})$  is relevant. In the present case the standard deviation at the global maximum of the von Mises stress is about 2.7% of the mean value. However, in case of a worst-case scenario study the extreme value is of higher interest. The value provided by the envelope indicates a deviation from the mean value corresponding to +6.3%, which is a factor of about 2.3 larger than the standard deviation.

#### 4.2.4. Effect of the turbulence intensity of the background turbulence

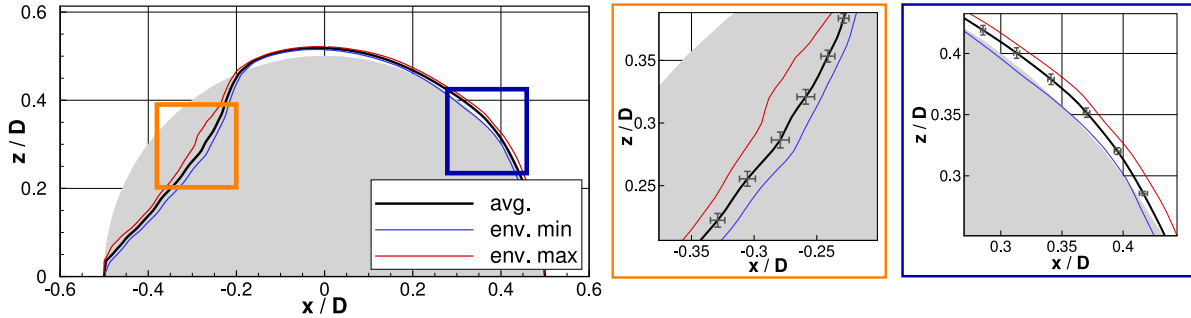
All previously presented simulations are carried out with a background turbulence of the same intensity. Based on the Reynolds stresses measured in Wood et al. (2016, 2018) and complemented by DNS data of Schlatter et al. (2009) this incoming background turbulence level  $Tu_{\text{STIG}}^0 = \sqrt{\frac{1}{3}(\overline{u'u'} + \overline{v'v'} + \overline{w'w'})}/u_\infty$  varies along the vertical axis  $z$  from 8% close to the bottom wall to below 1% in the free-stream flow. A question that remains is what influence does the value of  $Tu_{\text{STIG}}$  have on the force coefficients, on the maximal deflection of the membrane and on the inner stress in the material during a gust impact? In order to investigate this issue, the original synthetic inflow data of FSI 0 are scaled by a constant factor  $\alpha = \{1.0, 1.5, 2.0, 2.5, 3.0, 5.0\}$  according to  $Tu_{\text{STIG}} = \alpha Tu_{\text{STIG}}^0$ , where  $\alpha = 1.0$  denotes the original case. Note that this measure solely comprises the velocity fluctuations and not the averaged flow. Consequently, the obtained background turbulence signals are in phase and only differ in terms of the amplitude of the fluctuations. Additionally, the same gust as before ( $A_g/u_\infty = 1$ ,  $L_g^z/D = 1$  and  $z_g/D = 4/8$ ) is injected at the same place without any time delay.

Figs. 19(a)–(d) present the force coefficients predicted with the scaled background turbulence signals before and after the injection of the gust. As expected the level of the incoming turbulence significantly affects the temporal evolutions of  $c_x$  and  $c_z$ . Increasing values of  $Tu_{\text{STIG}}$  lead to a decrease of  $c_x$ . Since this trend is not so obvious in the time histories, Fig. 19(e) depicts the time-averaged value of  $c_x$  versus the parameter  $\alpha$ . Here the drag reduction is clearly visible. This observation can be explained by the reduction of the recirculation area behind the bluff body when  $Tu_{\text{STIG}}$  increases. Physically it means that the increased turbulence level leads to an earlier transition of the laminar boundary layer on the hemisphere. The evolving turbulent boundary layer can withstand the adverse pressure gradient over a longer distance. Thus, the separation in the vicinity of the apex of the hemisphere is shifted downstream. This phenomenon seems to be independent on the presence of the gust. The major part of the vertical force coefficient  $c_z$  can

<sup>2</sup> For a sample containing  $N$  value  $x_i$  the corrected sample standard deviation is  $\sqrt{\frac{1}{N-1} \sum_{i=1}^N (x_i - \bar{x})^2}$ .

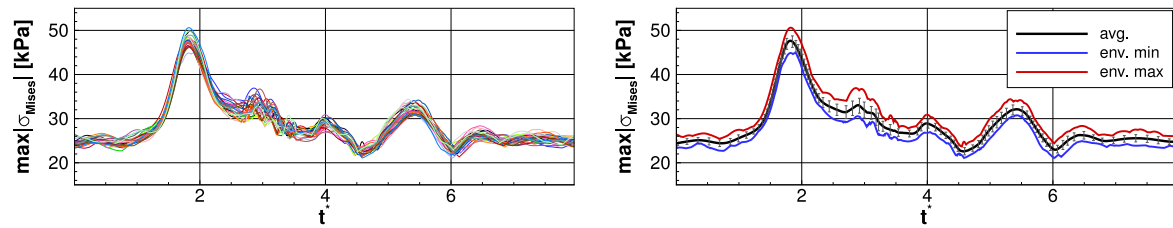


(a) Superposition of the results obtained by 25 simulations.



(b) Averaged deflection with its envelope and corrected standard deviations for  $x$ - and  $z$ -deflections.

Fig. 17. Background turbulence effect on flexible case ( $z_g^0/D = 4/8$ ,  $A_g/u_\infty = 1.0$ ,  $L_g^z/D = 1.0$ ): Maximal membrane deflections in the symmetry plane  $y = 0$  obtained with gusts injected at different time instants.



(a) Superimposed results obtained by 25 simulations. (b) Averaged  $\max(\sigma_{Mises})$  with its envelope and corrected standard deviations.

Fig. 18. Background turbulence effect on flexible case ( $z_g^0/D = 4/8$ ,  $A_g/u_\infty = 1.0$ ,  $L_g^z/D = 1.0$ ): Maximal von Mises stress values  $\max(\sigma_{Mises})$  obtained by gusts injected at different time instants.

be attributed to the zone of low pressure located in the acceleration area at the apex of the hemisphere (see Fig. 15(b)). This acceleration area does not change significantly with the increase of  $Tu_{STIG}$ , which explains the limited effect of  $Tu_{STIG}$  on  $c_z$  (see Figs. 19(b) and (d)).

The maximal membrane deflections obtained for a gust superimposed by background turbulence of different turbulence intensities are compared in Fig. 19(g). For a factor  $\alpha$  below 3.0 the maximally deflected shapes are close to each other. For the factors  $\alpha = \{3.0, 5.0\}$  the flexible structure is slightly less deflected than the reference case, which can be correlated with the decrease of the streamwise force coefficient  $c_x$ . Despite its large variation the level of the turbulence intensity  $Tu_{STIG}$  seems to be of minor importance for the membrane deflections compared to the issue at which point in time the gust is superimposed by the turbulent inflow data. To explain the minor effect of  $Tu_{STIG}$  the mass flow rate going through a restricted cross-section is evaluated. The area of interest is located around the centerpoint of the gust injection in the  $y - z$ -plane and is defined by  $-0.5 \leq y/D \leq 0.5$  and  $0 \leq z/D \leq 1$ . Furthermore, it is positioned just after the gust injection volume at  $x/D = -1$ . Fig. 20 shows that the mass flow rates induced by a gust superimposed by the background turbulence of

different intensities are very similar. Additionally, the mass flow rates for the pure background turbulence cases are depicted, which confirm that the synthetic turbulence inflow generator is designed to induce no additional mass fluxes. Consequently, even the increase of  $Tu_{STIG}$  superimposed on the gust does not modify the mass flow rates. This observation explains why the maximal deflections of the structure are so close to each other. In conclusion, the direct effect of the incoming turbulence on the fluid flow and the indirect influence on the structure have to be distinguished.

Additionally, for every level of the turbulence intensity the maximal von Mises stress predicted at each time step is compared in Fig. 19(f). Taking into account that solely the global maximal value of  $\max(\sigma_{Mises})$  is relevant for the worse-case scenario, the results obtained with the factors  $\alpha = \{1.0, 1.5, 2.0, 2.5, 3.0\}$  are close together. For the highest turbulence intensity of  $Tu_{STIG} = 5Tu_{STIG}^0$  this maximum is even smaller. Similar to the observation on the maximal membrane deflections, the increase of the turbulence intensity  $Tu_{STIG}$  leads to a stagnation or a diminution of the inner stresses occurring in the structure. Consequently, no new worst case is generated.

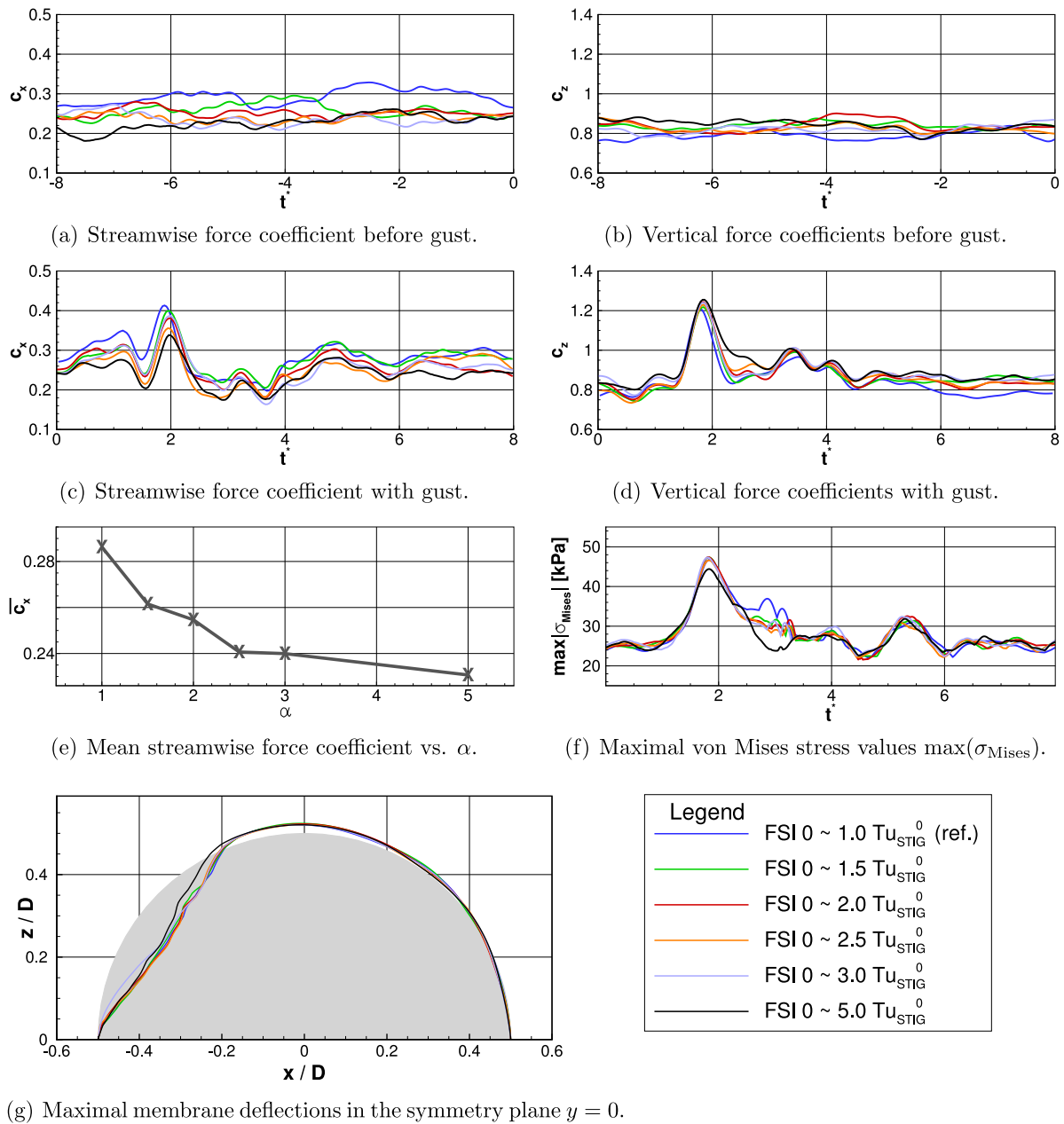


Fig. 19. Background turbulence effect on flexible case ( $z_g^0/D = 4/8$ ,  $A_g/u_\infty = 1.0$ ,  $L_g^z/D = 1.0$ ): Results obtained with gusts injected on underlying  $L_g^z$  background turbulence of different intensities.

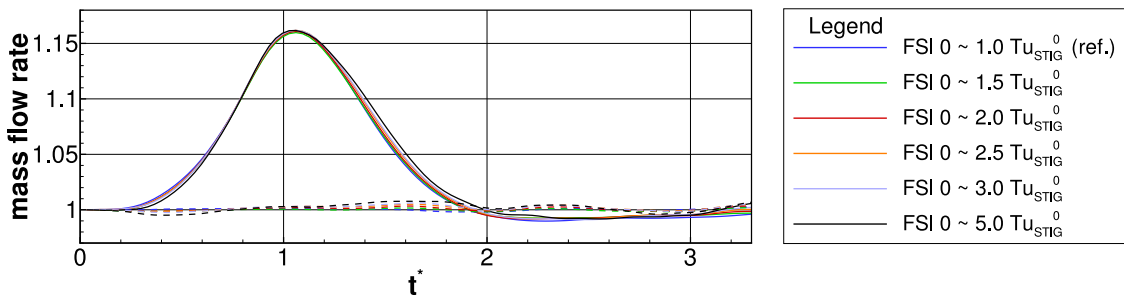


Fig. 20. Background turbulence effect on flexible case ( $z_g^0/D = 4/8$ ,  $A_g/u_\infty = 1.0$ ,  $L_g^z/D = 1.0$ ): Integrated mass fluxes through a vertical  $y$ - $z$ -plane normalized by its values at  $t^* = 0$  (Solid lines: Incoming background turbulence including a gust; Dashed lines: Incoming background turbulence only).

**Table A.2**  
Wind gusts at 10 m height over plane and free ground (Friederichs et al., 2009).

| Type of gust    | Gust velocity threshold |         | Appearance of wind effects       |   |
|-----------------|-------------------------|---------|----------------------------------|---|
|                 | [m/s]                   | [km/h]  | on a tree                        | on land   |
| Near gale       | > 14                    | > 50    | Whole trees move                 | Wind impedes walking                                |
| Gale            | 18–24                   | 65–90   | Branches Starts to break         | Windblown dust                                      |
| Storm           | 25–28                   | 90–100  | Pushes over shallow-rooted trees | Light damage (weak roof)                            |
| Violent storm   | 29–32                   | 100–120 | Big branch breaks                | Light damage (windows)                              |
| Hurricane force | > 33                    | > 120   | Mature trees uprooted            | Moderate damage (roof)<br>Devastating damage (wall) |

## 5. Conclusions

The effect of strong wind gusts impacting a lightweight civil engineering structure are investigated based on coupled high-fidelity FSI predictions. Such short-term highly instantaneous loads are crucial for the structural integrity. To determine the worst-case scenario meta-models and optimization approaches can be applied which require a certain amount of data to be obtained by time-consuming coupled simulations. In order to better understand the influence of the most relevant input parameters such as the gust strength, its length and impact position, a parameter study is carried out. It relies on discrete wind gusts, the superposition of stochastic background turbulence and a flexible as well as a rigid structure, where the latter is applied to fathom the possibility of reducing the computing time by this physical meta-model. The following main conclusions can be drawn:

- The streamwise force coefficient possesses two local extrema, the first when the gusts impacts the structure and the second when the gust departs from the structure leading to a region of low pressure on the backside. That astonishingly induces a force which is even higher than during the impact. The observation is valid for both the rigid and the flexible structure.
- The energy included in the gust increases with its length. Thus, longer gusts of the same gust strength lead to stronger forces on the structure.
- The trends concerning the effect of the gust injection height on the fluid forces are more complex and slightly differ between the rigid and flexible model. The streamwise force during the impact is augmented when the gust is closer to the bottom wall. This observation is valid for both structures. On the contrary, the streamwise force predicted on the rigid body during the departure of the gust possesses a clear maximum when the gust hits the hemisphere in the middle. For the membrane the streamwise force during the departure continues to increase for decreasing gust heights.
- The vertical force acting on the rigid body increases by decreasing the injection height and then reaches an upper limit. Contrary to the rigid case the vertical force on the flexible membrane has a maximum for gusts injected in the middle.
- These observations concerning the force coefficients show that the investigated generic lightweight FSI case cannot be reliably predicted by simulations based on the rigid structure. A two-way coupling is necessary here.
- In case of the flexible structure the maximal deflections of the membrane are found for gusts impacting the structure in the middle. For lower injection heights the membrane reaches nearly the same maximally deflected shape. The largest principal strains are observed for the lowest gust injection height.
- The maximum von Mises stress, which is of major interest for the worst-case scenario, is found again for the lowest injection height. It appears in the indentation near the bottom wall. For all cases a zone of high von Mises stresses forms at the periphery of the indentation and particularly at its top. The material in this area should be consolidated.

- Since in reality there is no discrete gust but the events are superimposed by background turbulence of the atmospheric boundary layer, the effect of this phenomenon was separately investigated. The deviations found in the peak values of the force coefficients ( $c_x$ ,  $c_z$ ) are about 19% and 14% for a turbulence intensity in the order of 8% close to the bottom wall ( $\alpha = 1$ ). The deflections of the membrane vary in the same order of magnitude. The maximal von Mises stress increases about 6%.
- The level of the turbulence intensity is found to directly affect the fluid flow around the structure. However, the strength of the turbulent fluctuations ( $\alpha = 1.5$  to 5) has a minor influence on the effect of the wind gust on the flexible structure, at least for the considered case, where the length scales of the background turbulence are about a factor of 50 smaller than the gust extension ( $L^{\text{STIG}}/D \approx 0.02$  vs.  $L_g^\xi/D = 1.0$ ). Under these circumstances an increase of the turbulence intensity does not generate a new worst case associated with the gust.

## CRedit authorship contribution statement

**G. De Nayer:** Conceptualization, Methodology, Software, Validation, Investigation, Visualization, Writing – original draft, Writing – review & editing. **M. Breuer:** Conceptualization, Methodology, Resources, Writing – original draft, Writing – review & editing, Supervision, Project administration, Funding acquisition.

## Declaration of competing interest

The authors declare that they have no known competing financial interests or personal relationships that could have appeared to influence the work reported in this paper.

## Data availability

Data will be made available on request.

## Acknowledgments

The project is financially supported by the *Deutsche Forschungsgemeinschaft*, Germany under the contract numbers BR 1847/17-1. Additionally, the authors want to thank the Chair of Structural Analysis of the Technical University of Munich for providing the computational structure dynamics solver Carat++ (Bletzinger et al., 2006) and the open-source coupling software EMPIRE (Sicklinger et al., 2014). Furthermore, the authors thank M. Klein (Universität der Bundeswehr München) for providing the original source code of the digital filter based inflow procedure.

## Appendix. Wind gust warnings of the German Weather Service (DWD)

See Table A.2

## References

- Andersen, S.J., Sørensen, J.N., 2018. Instantaneous response and mutual interaction between wind turbine and flow. *J. Phys.: Conf. Ser.* 1037 (7), 072011.
- Apostolatos, A., De Nayer, G., Bletzinger, K.U., Breuer, M., Wüchner, R., 2019. Systematic evaluation of the interface description for fluid–structure interaction simulations using the isogeometric mortar-based mapping. *J. Fluids Struct.* 86, 368–399.
- Basar, Y., Weichert, D., 2013. *Nonlinear Continuum Mechanics of Solids: Fundamental Mathematical and Physical Concepts*. Springer Science & Business Media.
- Bletzinger, K.U., Wüchner, R., Kupzok, A., 2006. Algorithmic treatment of shells and free form-membranes in FSI. In: Bungartz, H.J., Schäfer, M. (Eds.), *Fluid-Structure Interaction*. In: *Lecture Notes in Computational Science and Engineering*, LNCSE, vol. 53, Springer, Heidelberg, pp. 336–355.
- Boulbrachene, K., De Nayer, G., Breuer, M., 2021. Assessment of two wind gust injection methods: Field velocity vs. split velocity method. *J. Wind Eng. Ind. Aerodyn.* 218, 104790.
- Breitenberger, M., Apostolatos, A., Philipp, B., Wüchner, R., Bletzinger, K.U., 2015. Analysis in computer aided design: Nonlinear isogeometric B-Rep analysis of shell structures. *Comput. Methods Appl. Mech. Engrg.* 284, 401–457.
- Breuer, M., 2018. Effect of inflow turbulence on an airfoil flow with laminar separation bubble: An LES study. *Flow Turbul. Combust.* 101 (2), 433–456.
- Breuer, M., De Nayer, G., Münsch, M., Gallinger, T., Wüchner, R., 2012. Fluid-structure interaction using a partitioned semi-implicit predictor-corrector coupling scheme for the application of large-eddy simulation. *J. Fluids Struct.* 29, 107–130.
- Burton, T., Sharpe, D., Jenkins, N., Bossanyi, E., 2001. *Wind Energy Handbook*. John Wiley & Sons.
- De Jonge, J.B., Vink, W.J., 1997. Gust load conditions for fatigue tests based on a continuous gust concept. In: *38th Structures, Structural Dynamics, and Materials Conference*, AIAA Paper. AIAA-97-1279.
- De Nayer, G., Apostolatos, A., Wood, J.N., Bletzinger, K.-U., Wüchner, R., Breuer, M., 2018a. Numerical studies on the instantaneous fluid–structure interaction of an air-inflated flexible membrane in turbulent flow. *J. Fluids Struct.* 82, 577–609.
- De Nayer, G., Breuer, M., 2020. A source-term formulation for injecting wind gusts in CFD simulations. *J. Wind Eng. Ind. Aerodyn.* 207, 104405.
- De Nayer, G., Breuer, M., Boulbrachene, K., 2022. FSI simulations of wind gusts impacting an air-inflated flexible membrane at  $Re = 100,000$ . *J. Fluids Struct.* 109, 103462.
- De Nayer, G., Breuer, M., Perali, P., Grollmann, K., 2019. Modeling of wind gusts for large-eddy simulations related to fluid–structure interactions. In: Salvetti, M., Armenio, V., Fröhlich, J., Geurts, B.J., Kuerten, H. (Eds.), *ERCOFTAC Series, Direct and Large-Eddy Simulation XI*, 11th Int. ERCOFTAC Workshop on Direct and Large-Eddy Simulation: DLES-11, May 29–31, 2017, Vol. 25. Springer Nature Switzerland AG 2019, Pisa, Italy, pp. 453–459.
- De Nayer, G., Schmidt, S., Wood, J.N., Breuer, M., 2018b. Enhanced injection method for synthetically generated turbulence within the flow domain of eddy-resolving simulations. *Comput. Math. Appl.* 75 (7), 2338–2355.
- Doubrawa, P., Churchfield, M.J., Godvik, M., Sirmivas, S., 2019. Load response of a floating wind turbine to turbulent atmospheric flow. *Appl. Energy* 242, 1588–1599.
- Durst, F., Schäfer, M., 1996. A parallel block-structured multigrid method for the prediction of incompressible flows. *Int. J. Numer. Methods Fluids* 22 (6), 549–565.
- EASA, 2020. Certification specifications for large aeroplanes CS-25.
- FAA, 2014. Federal aviation regulations, part 25: Airworthiness standards: Transport category airplanes, section 341: Gust and turbulence loads, AC-25.341.
- Fidkowski, K., Kroo, I., Willcox, K., Engelson, F., 2008. Stochastic gust analysis techniques for aircraft conceptual design. In: *12th AIAA/ISSMO Multidisciplinary Analysis and Optimization Conference AIAA-2008-5848*. 10–12 Sept. 2008, Victoria, British Columbia Canada.
- Fonte, F., Ricci, S., Mantegazza, P., 2015. Gust load alleviation for a regional aircraft through a static output feedback. *J. Aircr.* 52 (5), 1559–1574.
- Fournier, E., Grihon, S., Bes, C., Klein, T., 2019. Prediction of preliminary maximum wing bending moments under discrete gust. *J. Aircr.* 56 (4), 1722–1725.
- Friederichs, P., Göber, M., Bentzien, S., Lenz, A., Krampitz, R., 2009. A probabilistic analysis of wind gusts using extreme value statistics. *Meteorol. Z.* 18 (6), 615–629.
- Goertz, S., Abu-Zurayk, M., Ilic, C., Wunderlich, T.F., Keye, S., Schulze, M., Kaiser, C., Klimmek, T., Süelözgen, Ö., Kier, T., et al., 2020. Overview of collaborative multidisciplinary design optimization activities in the DLR project VicToria. In: *AIAA Aviation 2020 Forum*. p. 3167.
- Guzman Nieto, M., ElSayed, M.S., Walch, D., 2019. Efficient global optimization and modal strain energy coefficient-based algorithm for fast prediction of dynamic aeroelastic loads. *Struct. Multidiscip. Optim.* 60 (2), 817–834.
- Heinrich, R., 2014. Simulation of interaction of aircraft and gust using the TAU-code. In: Dillmann, A., Heller, G., Krämer, E., Kreplin, H.-P., Nitsche, W., Rist, U. (Eds.), *New Results in Numerical and Experimental Fluid Mechanics IX: Contributions to the 18th STAB/DGLR Symposium*. Stuttgart, Germany, 2012, Springer International Publishing, Cham, pp. 503–511.
- Heinrich, R., Reimer, L., 2017. Comparison of different approaches for modeling of atmospheric effects like gusts and wake-vortices in the CFD code TAU. In: *International Forum on Aeroelasticity & Structural Dynamics*.
- Hoblitz, F.M., 1988. *Gust Loads on Aircraft: Concepts and Applications*. AIAA Education Series, Washington D.C..
- Huntley, S.J., Jones, D., Gaitonde, A., 2017. Aeroelastic gust response of an aircraft using a prescribed velocity method in viscous flows. In: *23rd AIAA Computational Fluid Dynamics Conference*. Denver, Colorado.
- IEC-Standard, 2002. 61400-21. Technical Report.
- Jones, J.G., 1973. *Statistical Discrete Gust Theory for Aircraft Loads: A Progress Report*. Royal Aircraft Establishment.
- Jones, J.G., 2004. Documentation of the Linear Statistical Discrete Gust Method AR-04. Technical Report, Citeseer, DOT/FAA.
- Jones, J.G., 2009. Nonlinear aircraft loads in severe atmospheric turbulence. *J. Aircr.* 46 (5), 1627–1633.
- Jones, D.R., Schonlau, M., Welch, W.J., 1998. Efficient global optimization of expensive black-box functions. *J. Global Optim.* 13 (4), 455–492.
- Kareem, A., 2008. Numerical simulation of wind effects: A probabilistic perspective. *J. Wind Eng. Ind. Aerodyn.* 96 (10), 1472–1497.
- Kareem, A., Wu, T., 2013. Wind-induced effects on bluff bodies in turbulent flows: Nonstationary, non-Gaussian and nonlinear features. *J. Wind Eng. Ind. Aerodyn.* 122, 21–37.
- Kelly, M., Andersen, S.J., Hannesdóttir, Á., 2021. Statistical impact of wind-speed ramp events on turbines, via observations and coupled fluid-dynamic and aeroelastic simulations. *Wind Energy Sci.* 6 (5), 1227–1245.
- Kemper, F.H., 2022. Prediction of gust induced cycle counts and fatigue damage of structures. *J. Wind Eng. Ind. Aerodyn.* 226, 105004.
- Khodaparast, H.H., Georgiou, G., Cooper, J., Riccobene, L., Ricci, S., Vio, G., Denner, P., 2012. Efficient worst case 1-cosine gust loads prediction. *J. Aeroelasticity Struct. Dyn.* 2 (3), 33–54.
- Klein, M., Sadiki, A., Janicka, J., 2003. A digital filter based generation of inflow data for spatially-developing direct numerical or large-eddy simulations. *J. Comput. Phys.* 186, 652–665.
- Knobloch, A., 2015. *Robust Performance Analysis for Gust Loads Computation* (Ph.D. thesis). Technische Universität Hamburg, Germany.
- Mann, J., 1998. Wind field simulation. *Probab. Eng. Mech.* 13 (4), 169–282.
- Mann, J., 2012. *Atmospheric Turbulence*. DTU Wind Energy, Technical University of Denmark, Denmark, DK-4000 Roskilde.
- Michalski, A., Gawenat, B., Gelenne, P., Haug, E., 2015. Computational wind engineering of large umbrella structures. *J. Wind Eng. Ind. Aerodyn.* 144, 96–107.
- Michalski, A., Kermel, P.D., Haug, E., Löhner, R., Wüchner, R., Bletzinger, K.-U., 2011. Validation of the computational fluid–structure interaction simulation at real-scale tests of a flexible 29 m umbrella in natural wind flow. *J. Wind Eng. Ind. Aerodyn.* 99 (4), 400–413.
- Nazzeri, R., Haupt, M., Lange, F., Sebastien, C., 2015. Selection of critical load cases using an artificial neural network approach for reserve factor estimation. In: *Deutscher Luft- Und Raumfahrt-Kongress*. Deutsche Gesellschaft für Luft- und Raumfahrt-Lilienthal-Oberth eV.
- Norris, S.E., Cater, J.E., Stol, K.A., Unsworth, C.P., 2010. Wind turbine wake modelling using large-eddy simulation. In: *Proceedings of the 17th Australian Fluid Mechanics Conference*. Curran Associates, Inc., University of Auckland, Australia.
- Patil, M., 2007. Nonlinear gust response of highly flexible aircraft. In: *48th AIAA/ASME/ASCE/AHS/ASC Structures, Structural Dynamics, and Materials Conference*. p. 2103.
- Philipp, B., Wüchner, R., Bletzinger, K.U., 2016. Advances in the form-finding of structural membranes. *Procedia Eng.* 155, 332–341.
- Piomelli, U., Chasnov, J.R., 1996. Large-eddy simulations: Theory and applications. In: Hallböck, M., Henningson, D.S., Johansson, A.V., Alfredson, P.H. (Eds.), *Turbulence and Transition Modeling*. Kluwer, pp. 269–331.
- Piqueu, J., García-Risco, A.Á., López, I., Breitsamter, C., Wüchner, R., Bletzinger, K.U., 2022. Numerical investigations of a membrane morphing wind turbine blade under gust conditions. *J. Wind Eng. Ind. Aerodyn.* 224, 104921.
- Porté-Agel, F., Wu, Y.T., Lu, H., Conzemi, R.J., 2011. Large-eddy simulation of atmospheric boundary layer flow through wind turbines and wind farms. *J. Wind Eng. Ind. Aerodyn.* 99 (4), 154–168.
- Raveh, D.E., 2011. Gust-response analysis of free elastic aircraft in the transonic flight regime. *J. Aircr.* 48 (4), 1204–1211.
- Reytier, T., Bes, C., Marechal, P., Bianciardi, M., Santgerma, A., 2012. Generation of correlated stress time histories from continuous turbulence power spectral density for fatigue analysis of aircraft structures. *Int. J. Fatigue* 42, 147–152.
- Ripepi, M., Verveld, M.J., Karcher, N.W., Franz, T., Abu-Zurayk, M., Görtz, S., Kier, T.M., 2018. Reduced-order models for aerodynamic applications, loads and MDO. *CEAS Aeronaut. J.* 9 (1), 171–193.
- Santo, G., Peeters, M., Van Paepegem, W., Degroote, J., 2020. Fluid-structure interaction simulations of a wind gust impacting on the blades of a large horizontal axis wind turbine. *Energies* 13 (3), 509.
- Schijve, J., 2003. Fatigue of structures and materials in the 20th century and the state of the art. *Int. J. Fatigue* 25 (8), 679–702.
- Schlatter, P., Orlu, R., Li, Q., Brethouwer, G., Fransson, J.H.M., Johansson, A.V., Alfredsson, P.H., Henningson, D.S., 2009. Turbulent boundary layers up to  $Re_\theta = 2500$  studied through simulation and experiment. *Phys. Fluids* 21 (5), 51702.
- Schmidt, S., Breuer, M., 2017. Source term based synthetic turbulence inflow generator for eddy-resolving predictions of an airfoil flow including a laminar separation bubble. *Comput. & Fluids* 146, 1–22.

- Scott, R.C., Pototzky, A.S., Perry III, B., 1993. Computation of maximized gust loads for nonlinear aircraft using matched-filter-based schemes. *J. Aircr.* 30 (5), 763–768.
- Sen, S., De Nayer, G., Breuer, M., 2017. A fast and robust hybrid method for block-structured mesh deformation with emphasis on FSI-LES applications. *Int. J. Numer. Methods Eng.* 111 (3), 273–300.
- Sicklinger, S., Belsky, V., Engelmann, B., Elmqvist, H., Olsson, H., Wüchner, R., Bletzinger, K.-U., 2014. Interface Jacobian-based co-simulation. *Int. J. Numer. Methods Eng.* 98 (6), 418–444.
- Singh, R., Baeder, J.D., 1997. Direct calculation of three-dimensional indicial lift response using computational fluid dynamics. *J. Aircr.* 34 (4), 465–471.
- Sitaraman, J., Baeder, J.D., 2006. Field velocity approach and geometric conservation law for unsteady flow simulations. *AIAA J.* 44 (9), 2084–2094.
- Smagorinsky, J., 1963. General circulation experiments with the primitive equations I: The basic experiment. *Mon. Weather Rev.* 91 (3), 99–165.
- Sørensen, P., Hansen, A.D., Rosas, P.A.C., 2002. Wind models for simulation of power fluctuations from wind farms. *J. Wind Eng. Ind. Aerodyn.* 90 (12), 1381–1402.
- Storey, R.C., Norris, S.E., Cater, J.E., 2013. Large eddy simulation of wind events propagating through an array of wind turbines. In: *Proceedings of the World Congress on Engineering*, vol. 3, London, UK.
- Storey, R.C., Norris, S.E., Cater, J.E., 2014. Modelling turbine loads during an extreme coherent gust using large eddy simulation. *J. Phys. Conf. Ser.* 524, 012177.
- Thompson, J.F., Warsi, Z.U.A., Wayne Mastin, C., 1985. *Numerical Grid Generation: Foundations and Applications*. vol. 45, North-Holland.
- Wales, C., Jones, D., Gaitonde, A., 2014. Prescribed velocity method for simulation of aerofoil gust responses. *J. Aircr.* 52 (1), 64–76.
- Wang, T., Wüchner, R., Sicklinger, S., Bletzinger, K.U., 2016. Assessment and improvement of mapping algorithms for non-matching meshes and geometries in computational FSI. *Comput. Mech.* 57 (5), 793–816.
- Wang, H., Zhang, Y.M., Mao, J.X., 2022. Sparse Gaussian process regression for multi-step ahead forecasting of wind gusts combining numerical weather predictions and on-site measurements. *J. Wind Eng. Ind. Aerodyn.* 220, 104873.
- Wang, H., Zhang, Y.M., Mao, J.X., Wan, H.P., 2020. A probabilistic approach for short-term prediction of wind gust speed using ensemble learning. *J. Wind Eng. Ind. Aerodyn.* 202, 104198.
- Wood, J.N., Breuer, M., De Nayer, G., 2018. Experimental studies on the instantaneous fluid–structure interaction of an air–inflated flexible membrane in turbulent flow. *J. Fluids Struct.* 80, 405–440.
- Wood, J.N., De Nayer, G., Schmidt, S., Breuer, M., 2016. Experimental investigation and large-eddy simulation of the turbulent flow past a smooth and rigid hemisphere. *Flow Turbul. Combust.* 97 (1), 79–119.
- Wu, Z., Cao, Y., Ismail, M., 2019. Gust loads on aircraft. *Aeronaut. J.* 123 (1266), 1216–1274.
- Zeiler, T.A., 1997. Matched filter concept and maximum gust loads. *J. Aircr.* 34 (1), 101–108.
- Zholtovski, S., Stephan, A., Holzäpfel, F., 2020. Towards virtual flight in realistic environments: A hybrid coupled simulation method. *AIAA J.* 58 (3), 1266–1277.